Particuology 115 (2026) 292–308

Contents lists available at ScienceDirect

Particuology

journal homepage: www.elsevier.com/locate/partic

Improvement of hard-sphere/pseudo-particle modeling (HS-PPM) for high Knudsen number gas-solid flows

Mingcan Zhao[a], Feiguo Chen[a], Yu Zhang[a], Chengxiang Li[a,c], Tianhao Qiu[b], Wei Ge[a,c,*]

[a] State Key Laboratory of Mesoscience and Process Engineering, Institute of Process Engineering, Chinese Academy of Sciences, Beijing, 100190, China
[b] School of Energy Science and Engineering, Harbin Institute of Technology (HIT), Harbin, 150001, China
[c] School of Chemical Engineering, University of Chinese Academy of Sciences, Beijing, 100049, China

HIGHLIGHTS

- HS-PPM is implemented with eliminated inlet-outlet coupling and triangular elements method for wall description.
- Simulation accuracy and efficiency are balanced for high Knudsen number situations.
- Temperature and flow fields of IRVE in rarefied gas are well predicted based on dimensionless numbers.
- The flow system of porous particle at atomic level can be simulated by the implemented HS-PPM.

GRAPHICAL ABSTRACT

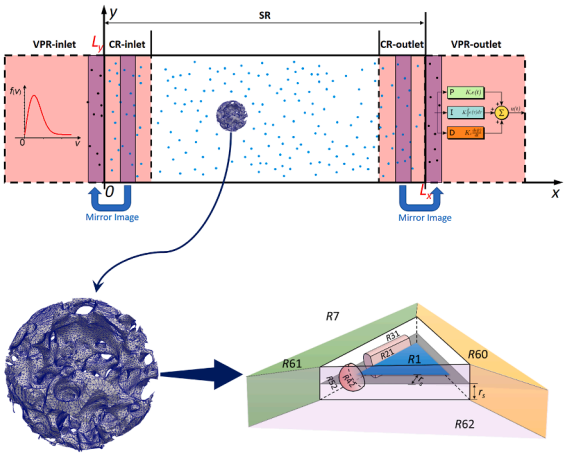

ARTICLE INFO

Keywords:
HS-PPM
Implicit boundary conditions
Triangular elements
Flow around porous particles
Rarefied gas
Supersonic flow

ABSTRACT

Hard-sphere/pseudo-particle modeling (HS-PPM) provides a parallel and more versatile implementation of molecular dynamics simulation based on hard-sphere model at large scales with remarkable performance. For more practical applications, however, more sophisticated and realistic boundary conditions have to be incorporated. In this work, the artifact of inlet-outlet coupling due to periodic boundary is basically eliminated by adding collisions at both ends and proportional-integral-differential (PID) control of density at the outlet based on implicit boundary conditions, maintaining reasonable flow field there for both high (up to 13.0) and low (down to 0.0) Mach numbers. Moreover, geometrically complex boundaries are approximated by a large number of polygonal (in particular, triangular) elements, instead of exact analytical descriptions, to balance the accuracy and efficiency. Given the challenges of nanoscale experimentation, the drag coefficients from simulation conducted at matching dimensionless numbers were compared with macroscopic results. With these improvements,

This article is part of a special issue entitled: SI honoring Profs. Jin & Yu published in Particuology.

* Corresponding author. State Key Laboratory of Mesoscience and Process Engineering, Institute of Process Engineering, Chinese Academy of Sciences, Beijing, 100190, China.
E-mail address: wge@ipe.ac.cn (W. Ge).

https://doi.org/10.1016/j.partic.2026.06.002
Received 12 February 2026; Received in revised form 16 May 2026; Accepted 1 June 2026
Available online 8 June 2026

the flow around a conical particle and the Inflatable Re-entry Vehicle Experiment (IRVE) was successfully simulated and demonstrated consistent to experiment and numerical results from direct simulation Monte Carlo (DSMC) towards the continuum flow limit (with the Knudsen number ranging from 0.1 to 1.7). Furthermore, the drag coefficient of nano-particles in fluid flow, which is challenging for experimental measurement, was obtained from simulation results, and the potential of HS-PPM in simulating particles and systems with complex structures is exemplified by the gas flow and diffusion in porous micro/nano-particles.

Nomenclature

A_j	Area of cell j, m^2
C_D	Drag coefficient
$\boldsymbol{c}_K$	Position of the inner center of triangular element, m
d_{HS}	Diameter of hard-sphere molecule, m
d_{PPM}	Diameter of pseudo-particle molecule, m
D	Characteristic length of the system, m
k_B	Boltzmann constant; 1.380649×10^{-23} J K^{-1}
K_P	Proportional coefficient of PID controller
K_I	Integral coefficient of PID controller
K_D	Derivative coefficient of PID controller
L_x	Length along the flow direction, m
m	Mass of molecule, kg
n_j	Number density in cell j, m^{-3}
N_j	Number of the accumulated concentration in cell j
$\boldsymbol{n}_K^i$	Position of the ith vertices of triangular element, m
$\boldsymbol{n}_{oK}^o$	Normal vector of triangular element, m
$\boldsymbol{o}_K^i$	The ith edge vector of triangular element, m
r_s	Molecular radius, m
R_n	Random number in accordance with standard normal distribution
Δt	Global simulation time step, s
T	Temperature, K
T_w	Wall temperature, K
T_0	Flow temperature at free stream, K
v_{mp}	Most probable speed, m s^{-1}
v_x	Velocity along the flow direction, m s^{-1}
v_T	Thermal velocity, m s^{-1}
$\boldsymbol{x}_S$	Molecular position, m
Kn	Knudsen number
Ma	Mach number
Re	Reynolds number
α	Thermal accommodation coefficient
ρ	Density, kg m^{-3}
η	Volume fraction
λ	Mean free path of molecules, m
θ	Half cone angle, °

Subscripts

0	Flow properties at free stream
j	Cell index
K	Triangular element
w	Wall
x	Flow direction

1. Introduction

With new developments in process engineering such as micro-chemical engineering (Shen et al., 2018; Sun et al., 2020; Suryawanshi et al., 2018; Tian et al., 2025; Zhu et al., 2017) and flow chemistry (Brzozowski et al., 2015; Ge et al., 2019; Gokul & Malaikannan, 2024; Tian & Wu, 2024; Wegner et al., 2012; Yakunchikov et al., 2025), detailed understanding and precise control of the reaction-diffusion-flow coupling as well as heat transfer is increasingly important. However, in systems where the mean free path of molecules (λ) is considerable, such as flying particles in rarefied gas, or where the characteristic scale of the flow field (D) is too small, such as flow in porous catalyst particles shown in Fig. 1, the Knudsen number (Kn), defined as the ratio of λ to D, increases and may exceed 0.1. In these high Kn situations, computational fluid dynamics (CFD) simulations relying on the Navier-Stokes equations yield unreliable or even invalid results due to the breakdown of continuum hypothesis (Qiu et al., 2022). On the other hand, molecular dynamics (MD) simulations, starting at micro scale, is infeasible in terms of computational costs for such systems (Hou et al., 2022; Hu et al., 2017; Tchipev et al., 2019; Watanabe et al., 2013). Direct simulation Monte Carlo (DSMC) is much faster than MD simulation under rarefied conditions, but becomes inaccurate for dense gases and highly non-equilibrium conditions, for example, shock waves (Chen & Boyd, 1996; Fedosov et al., 2004; Moss et al., 2006; Plotnikov & Shkarupa, 2010, 2012).

In searching for a more accurate and yet efficient simulation method for high Kn gas flows, it is noted that MD simulation based on the soft-sphere (SS) models is inefficient and cost-prohibitive for redundant computations, such as excess status updates in the interval of collisions. On the other hand, MD simulation based on the hard-sphere (HS) model adopts event-driven scheme, wherein specific molecular information (position, velocity, etc.) will not be updated unless the instantaneous collision event happens, thus the unnecessary computation between the event is avoided. The physical properties of HS systems can be predicted by Chapman-Enskog theory (Chapman & Cowling, 1970; Pieprzyk et al., 2024; Wu et al., 2015, 2016), and the simulated hydrodynamic behaviors are also consistent with those results predicted by computational fluid dynamics (Akkaya & Kandemir, 2015; Kandemir & Sevilgen, 2008; Ramirez et al., 2000; Scalas et al., 2015; Zhang et al., 2016b). These results demonstrate that the HS model is reliable for systems dominated by repulsive interactions. However, the parallelization of event-driven scheme faces fundamental challenges, as conventional approaches like the rollback algorithm frequently exhibit diminished parallel efficiency despite their straightforward implementations (Marin, 1997; Zhang et al., 2016b).

Considering the advantages of SS and HS models, pseudo-particle modeling (PPM) that combines the instantaneous collision of HS systems and time-driven scheme of SS systems was proposed (Ge & Li, 2001, 2003). All pseudo-particles (PPs) are advanced in uniform time steps, followed by overlap detection between PPs in neighboring cells and subsequent collision treatment of overlapping pairs. Hence, the low efficiency of SS models under rarefied conditions and the parallelization difficulties of HS model are all avoided (Ge & Li, 2001, 2003). However, molecular overlaps may lead to the deviations of the simulated states between HS and PPM. Therefore, the nominal diameter, defined as the diameter of PPs used in the simulations, was numerically determined to map the properties of the PPs to those of the HSs (Chen & Ge, 2010). The exchange sequence of boundary information was designed to enable parallel simulations using the message

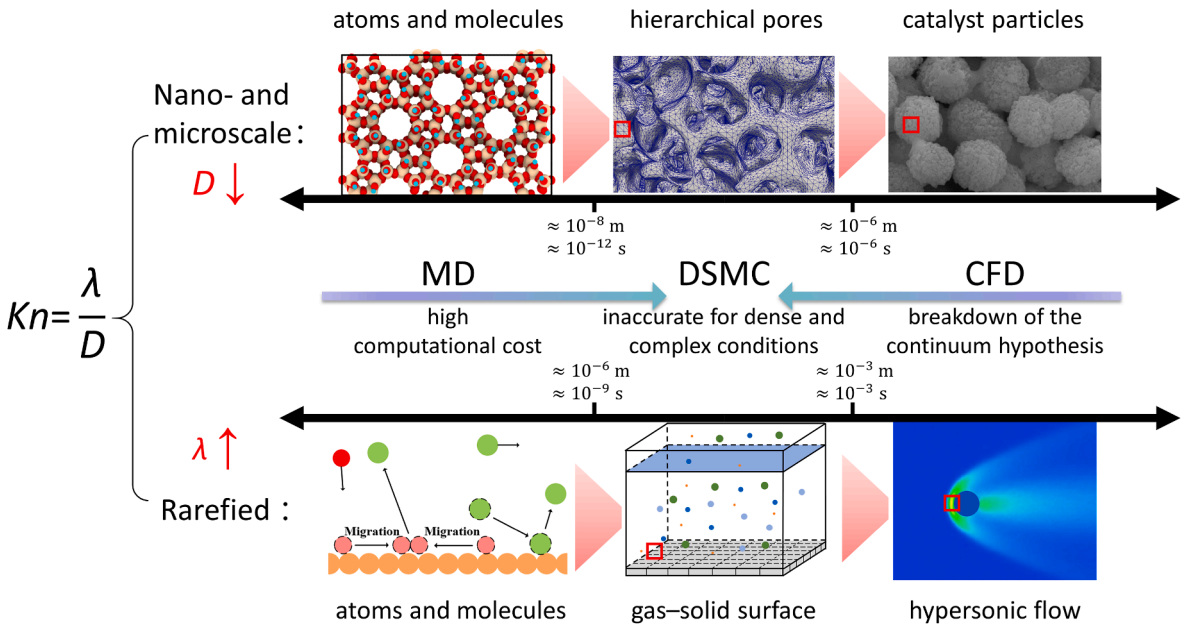

Fig. 1. Typical high Knudsen number scenarios and their corresponding simulation models.

passing interface (MPI) (Lu et al., 2009). Furthermore, the strategic replacement of HSs with PPs in boundary regions (Fig. 2) enables independently computation of HSs within each sub-domain and achieving near perfect parallelization scalability, which is called hard-sphere/pseudo-particle modeling (HS-PPM) (Zhang et al., 2016b). HS-PPM has been further extended to gas-solid multiscale flow and validated by HS simulations (Li et al., 2017a, 2017b, 2019; Zhang et al., 2016b), and showed promising prospect in balancing computational efficiency and numerical accuracy for high *Kn* gas flows.

When the rarefied gas flow is caused by the relative motion of solid objects instead of apparent pressure difference (Ma et al., 2019; Zhang et al., 2016a; Zhao et al., 2019), the traditional periodic boundary conditions are unable to maintain translational velocity and uniform density at the inlet. Partly decoupling the boundary by reallocating the outflow molecules at the inlet while keeping a constant molecule number (free stream inlet/outlet conditions) also deviates from the real density conditions (Ma et al., 2019). Implicit treatment for flow boundaries proposed by Akkaya et al. demonstrates remarkable performance (Akkaya & Kandemir, 2015; Liou & Fang, 2000; Shah et al., 2018), while the addition of molecules at the outlet relies on known properties which is unrealistic in the simulation of flow over moving bodies. Moreover, neglecting the collision effects of newly incorporated boundary molecules may lead to boundary instability and reduce the physical fidelity of the simulation. Besides the boundary conditions, HS-PPM suffers the common difficulty of particle methods in resolving complex boundaries analytically (Cheng, 2009; Kosyanchuk & Yakunchikov, 2018; Ramirez, 2017; Yakunchikov & Kosyanchuk, 2018, 2019a, 2019b). Describing irregular surfaces with static molecules for higher accuracy requires smaller radius and hence larger-amount of boundary molecules (Zhang et al., 2016a), resulting in reduced simulation efficiency and accuracy. Therefore, it is imperative to develop a completely decoupled inlet and outlet boundary settings that can realize uniform flow without pressure difference, as well as an efficient method for wall description. Both advancements are crucial for extending the applicability of HS-PPM in the simulation of high Knudsen number gas flows, and bridging the gap between CFD and MD simulations.

Thus, this work develops two critical enhancements to HS-PPM: (i) a fully decoupled inlet/outlet boundary condition with PID control that eliminates the inlet-outlet coupling artifact and works without knowing outlet properties, and (ii) a triangular element method that can handle arbitrarily complex geometries without analytical formulations. Compared to DSMC, HS-PPM retains molecule-level accuracy while offering better scalability in the near-end region; compared to previous HS-PPM implementations, the new boundary condition enables uniform flow with zero pressure gradient, and the triangular-element method extends applicability to porous particles and reentry vehicles. In Section

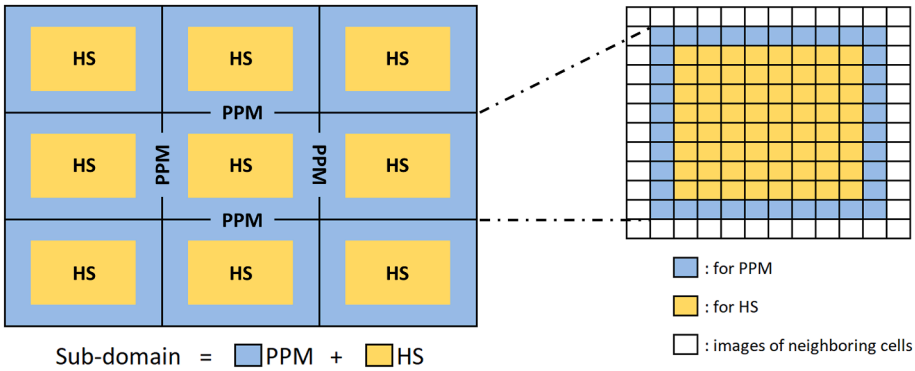

Fig. 2. Framework of the HS-PPM approach (reprinted from Zhang et al., 2016b).

2, The concentration control region (CR) and virtual particle region (VPR) were set for both inlet and outlet to add molecules and collisions, and proportional integral differential (PID) control was adopted at the outlet to adjust the density gradient in simulations of flow over bodies. The wall was finitely discretized into triangular elements (Kremmer & Favier, 2001a, 2001b) and the interaction between the gas molecule with the wall was described by the collision between the molecule and the triangle elements. In Section 3, the inlet/outlet boundary condition with PID control was validated in the simulation of uniform flow, and the triangular elements method was verified in the simulation of flow around a conical particle and the Inflatable Re-entry Vehicle Experiment (IRVE) under transition flow conditions (Lindell et al., 2006; Moss et al., 2006; O'Keefe & Bose, 2010; Olds et al., 2013; Wu et al., 2022). Finally, the enhanced boundary and wall surface treatments were used to simulate the flow around a spherical porous particle.

2. Methods

The basic structure of the HS-PPM is illustrated in Fig. 2 for a 2D illustration. We employed a hybrid modeling approach where the seamless integration of HS and PPM for each MPI process is realized through domain decomposition. For each sub-domain, the intra-process collisions are governed by the HS model (yellow region), while the inter-process interactions in boundary regions are handled by the PPM model (blue region). The HS sub-regions are isolated by time-driven PPM boundaries, and the width of PPM region must exceed twice the diameter of the largest molecule to prevent inter-process interference.

The detailed process, depicted in Fig. 3, consists of two main modules: the first part for HS simulations and the other for PPM simulations. For each PPM time step, multiple events in the HS region are first handled, followed by the subsequent execution of updates, collisions, and boundary transfers within the PPM region. By taking full advantage of the PPM model, this approach successfully enables the parallelization of the HS model, which is hindered by inherent concurrency constraints.

Boundary condition modifications and wall descriptions in this work, including addition of molecule/collision and PID control, were incorporated into the HS-PPM sub-modules while preserving the core computational workflow, as shown in Fig. 3.

2.1. The zero gradient outlet boundary conditions

The simulation domain consists of a simulation region (SR) and virtual particle regions (VPR), as shown in Fig. 4. VPR are set at both inlet ($x = 0$) and outlet ($x = L_x$). Control regions (CR) are established within the SR to implement the inlet and outlet conditions. Molecules and collisions are added at the boundary between the CR and VPR.

2.1.1. Addition of molecules at inlet

At the inlet, the density, temperature, and translational velocity of gas are considered constant, and denoted by:

$$\begin{cases} \rho|_{x=0} = \rho_c \\ T|_{x=0} = T_c \\ v_x|_{x=0} = v_c \end{cases} \tag{1}$$

The accumulated concentration, N_j, was monitored to determine the need for molecule addition at the inlet (Eq. (2)). The velocity of added molecules follows a Maxwellian distribution at the specified temperature in the y- and z-directions, whereas a biased-Maxwellian distribution is followed in the x-direction (Eq. (3)). The position of molecules was randomly assigned in y- and z-directions and calculated by $v_x \cdot \Delta t$ in x-direction.

$$\begin{cases} N_j &= F_j \Delta t A_j \\ F_j &= \dfrac{n_j}{2\sqrt{\pi}\beta_j}\left\{\exp\left(-s_j^2\cos^2\phi\right) + \sqrt{\pi}\, s_j \cos\phi\left[1+\operatorname{erf}\left(s_j\cos\phi\right)\right]\right\} \\ s_j &= v_{x,j}\beta_j \\ \beta_j &= \dfrac{1}{v_{\mathrm{mp},j}} = \dfrac{1}{\sqrt{\dfrac{2k_B T_j}{m}}} \end{cases} \tag{2}$$

where subscript j is the number of cells, A_j is the area of cell j, n_j is the molecule density in cell j, T is the temperature, ϕ is 0 for upstream and π for downstream boundary, and v_{mp} is the most probable speed.

$$\begin{cases} v_x &= v_{x,j} - f\left(\dfrac{v_{x,j}}{v_{\mathrm{mp}}}\right) v_{\mathrm{mp}} \\ v_y &= v_{y,j} + v_{\mathrm{mp}}\dfrac{R_{n,1}}{\sqrt{2}} \\ v_z &= v_{z,j} + v_{\mathrm{mp}}\dfrac{R_{n,2}}{\sqrt{2}} \end{cases} \tag{3}$$

where R_n is random number generated from standard normal distribution, f is the function of acceptance-rejection method (Akkaya & Kandemir, 2015).

2.1.2. Addition of molecules at outlet

Defining the outlet condition is challenging due to the anisotropic changes in the flow field across all three directions following gas-wall interactions. To reproduce the real outlet condition, the properties such as molecule density, temperature, and velocity in the first layer at VPR-outlet are set identical to the adjacent CR-outlet cell, i.e., the zero gradient condition denoted as:

$$\begin{cases} \dfrac{\partial \rho}{\partial x}\Big|_{x=L} = 0 \\ \dfrac{\partial T}{\partial x}\Big|_{x=L} = 0 \\ \dfrac{\partial v_x}{\partial x}\Big|_{x=L} = 0 \end{cases} \tag{4}$$

Due to the random fluctuation of the molecule density in these cells, zero gradient condition may cause positive feedback, that means excessive added molecules in the CR caused by fluctuation will result in an accumulation of molecules in the adjacent VPR, which in return, will further lead to the rise of concentrations in CR. Hence, PID control was adopted and the concentration gradient in the last five-layer cells close to the outlet was selected as the controlling variable to eliminate the positive feedback effect caused by zero gradient boundary condition. The proportional, integral (time-averaged), and derivative coefficients were initially set to −1 and then manually fine-tuned based on the amplitude and period of density fluctuations. The final values were adjusted to −1, −10, and 0, respectively. These settings were applied uniformly throughout our simulations and were found to be appropriate within the tested parameter range. It should be noted that the PID parameters are expected to have a quantitative relationship with the operating conditions, however, this aspect has not been investigated in the current study.

2.1.3. Addition of collisions at inlet and outlet

Additionally, collisions were added in VPR regions using mirror image (purple layer in Fig. 4) at the inlet and outlet. The molecule information in the second-layer grids in the CR close to the inlet and outlet

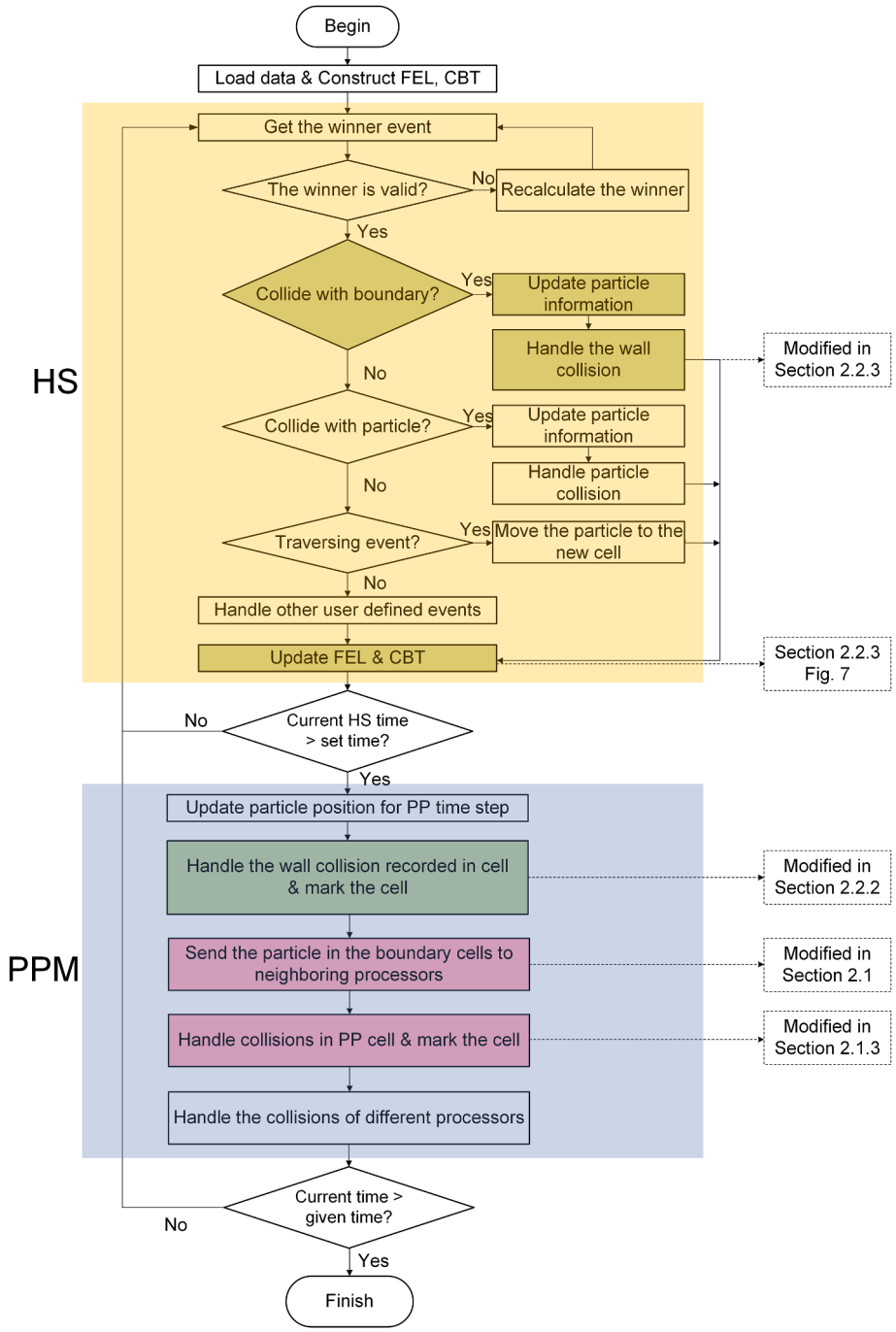

Fig. 3. Algorithm flow chart of the improved HS-PPM approach. FEL is the abbreviation of future event list and CBT is the abbreviation of complete binary tree. The modules shown in pink and green illustrate the modifications on the boundary conditions in section 2.1 and the handling of complex wall by triangular elements in section 2.2, respectively.

were copied to the corresponding VPR as mirror image (black molecules in Fig. 4) to provide collisions with the first-layer grids in CR. The molecules in the VPR were deleted simultaneously after collision, thus exert no influence on the real molecules from which they were mirrored.

2.2. Triangular elements method

2.2.1. Triangular elements

Triangular elements stored in cells were employed to describe the complex wall (Kremmer & Favier, 2001a) (Fig. 5). Each triangular element has three vertexes $\boldsymbol{n}_{\mathrm{K}}^{i}$, the inner center of the triangular is labeled as $\boldsymbol{c}_{\mathrm{K}}$, the normal vectors are denoted by $\boldsymbol{n}_{\mathrm{oK}}^{\mathrm{o}}$, and the three edge vectors are shown in Eq. (5).

$$\begin{aligned}\boldsymbol{o}_{\mathrm{K}}^{1}&=\boldsymbol{n}_{\mathrm{K}}^{2}-\boldsymbol{n}_{\mathrm{K}}^{1}\\ \boldsymbol{o}_{\mathrm{K}}^{2}&=\boldsymbol{n}_{\mathrm{K}}^{3}-\boldsymbol{n}_{\mathrm{K}}^{2}\\ \boldsymbol{o}_{\mathrm{K}}^{3}&=\boldsymbol{n}_{\mathrm{K}}^{1}-\boldsymbol{n}_{\mathrm{K}}^{3}\end{aligned} \tag{5}$$

The vertical vectors from the center of triangular elements towards the three edges are given by:

$$\boldsymbol{o}_{\mathrm{gK}}^{i}=\boldsymbol{n}_{\mathrm{K}}^{i}+\left[\left(\boldsymbol{c}_{\mathrm{K}}-\boldsymbol{n}_{\mathrm{K}}^{i}\right)\left(\boldsymbol{o}_{\mathrm{K}}^{i}\right)^{O}\right]\left(\boldsymbol{o}_{\mathrm{K}}^{i}\right)^{O}-\boldsymbol{c}_{\mathrm{K}} \tag{6}$$

The relative vector from the center of sphere with centroid at $\boldsymbol{x}_s$ and radius of r_s is:

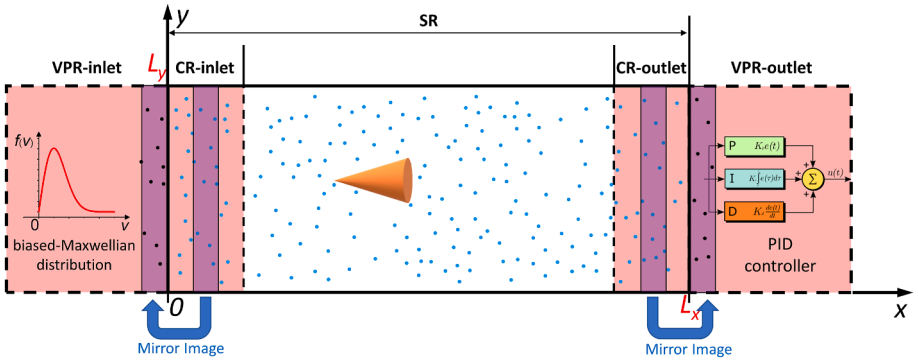

Fig. 4. Illustration of the new boundary condition settings. The cone geometry depicted here serves as an illustrative example and can be substituted with other objects.

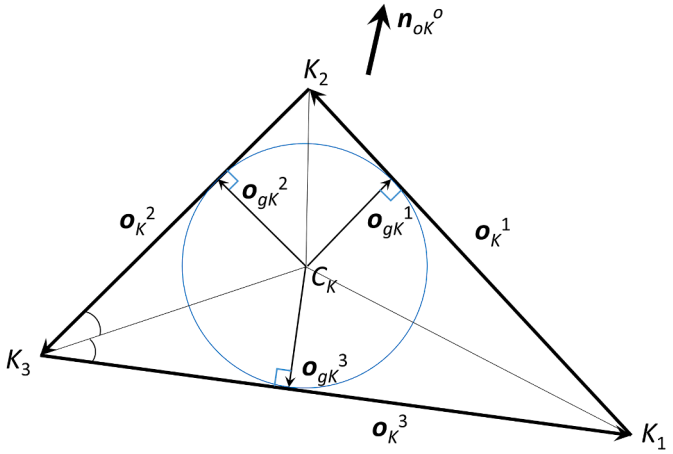

Fig. 5. Illustrations for triangular elements (Kremmer & Favier, 2001a).

$$\boldsymbol{v}_{\mathrm{C}} = \boldsymbol{x}_{\mathrm{S}} - \boldsymbol{c}_{\mathrm{K}} \tag{7}$$

Each triangular element was extended in both positive and negative normal directions by the length of r_s to infinite surfaces and the two extended surfaces form an infinite thin layer with total thickness of $2r_s$ (Fig. 6a). A concentric extended triangular element was built by extending the basic triangular element by r_s in the directions of vertical vectors from the center towards the three edges. The two triangular elements were further extended to two triangular prisms with the height of $2r_s$ inside the infinite thin layer (Fig. 6a). The infinite thin layer was then divided into 7 parts (R1-R7) by the two triangular prisms and some auxiliary lines (Fig. 6). The seven parts were named in the order of near-to-far from the basic triangular element (Fig. 6a and Table 1). A collision between a molecule and a triangular element is determined by checking for contact between the molecule centroid and any of the seven component regions.

2.2.2. *Molecule collides with triangular elements in PPM region*

In the PPM region, the collision between the molecule and the triangle element is determined by the relative position at each time step. Accordingly, determining the sub-region of a molecule is a prerequisite for checking its collisions within the PPM region.

The distance l between the centroid of molecule and the triangular element is calculated by:

$$a = \boldsymbol{v}_{\mathrm{C}}(\boldsymbol{n}_{\mathrm{oK}})^{O} \tag{8}$$

$$l = |a| - r_S \tag{9}$$

If $l > 0$, the molecule locates in the R7 sub-region and does not overlap with the triangular element.

If $l < 0$, the projection of the molecule on the surface $\boldsymbol{x}_{\mathrm{c}}$ is calculated by Eq. (10), while the relative vector of $\boldsymbol{x}_{\mathrm{c}}$ away from the incenter is $\boldsymbol{v}_{\mathrm{xc}}$, as defined by Eq. (11). The sub-region where the molecule projection $\boldsymbol{x}_{\mathrm{c}}$ locates is then determined by calculating the angle acos (b_{i}) between $\boldsymbol{v}_{\mathrm{xc}}$ and $\boldsymbol{o}_{\mathrm{gk}}$ given by Eq. (12).

$$\boldsymbol{x}_{\mathrm{C}} = \boldsymbol{x}_{\mathrm{S}} - a(\boldsymbol{n}_{\mathrm{oK}})^{O} \tag{10}$$

$$\boldsymbol{v}_{\mathrm{xC}} = \boldsymbol{x}_{\mathrm{C}} - \boldsymbol{c}_{\mathrm{K}} \tag{11}$$

$$b_i = (\boldsymbol{v}_{\mathrm{xC}})^{O}\left(\boldsymbol{o}_{\mathrm{gK}}^{i}\right)^{O} \tag{12}$$

The projection of $\boldsymbol{v}_{\mathrm{xc}}$ on $\boldsymbol{o}_{\mathrm{gk}}$ and the minimum angle in the sub-region is used to determine whether the molecule overlaps with the sub-region i. If the projection satisfies Eq. (13), the molecule is in the sub-region R1 and overlaps with the triangular element. If the projection satisfies Eq. (14), the molecule locates in the sub-region R6x, and there is no overlap between the molecule and triangular element.

$$b_i|\boldsymbol{v}_{\mathrm{xC}}| < \left|\boldsymbol{o}_{\mathrm{gK}}^{iSub}\right| \tag{13}$$

$$b_i|\boldsymbol{v}_{\mathrm{xC}}| > \left|\boldsymbol{o}_{\mathrm{gK}}^{iSub}\right| + r_{\mathrm{s}} \tag{14}$$

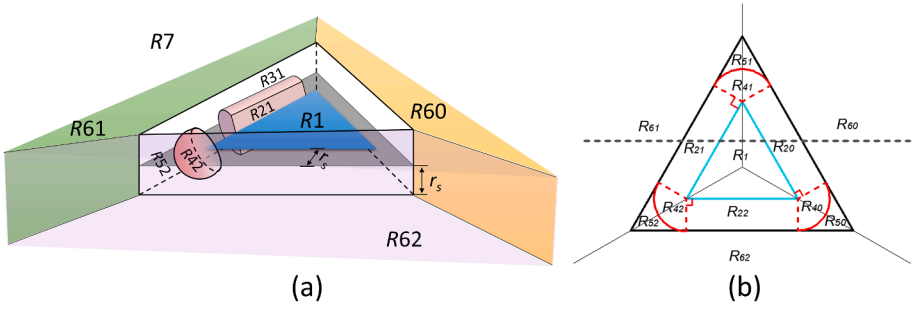

Fig. 6. Illustration of parts R1-R7 for handling the collision between molecule and the triangular element. (b) Is the cross section of (a) at the surface that the basic triangular element belongs to. The blue lines in (b) represent the edges of basic triangular element and the black bold lines represent the edges of the extended triangular prism. The solid red lines represent the edges of the sphere centered at the vertex of basic triangular element with a radius of r_s. The interpretations for the seven parts are listed in Table 1.

Table 1
Division of the infinite thin layer extended from the triangular element.

Locations	Region	Extra description
Inside the basic triangular prism	R1	Distance to the triangular element is less than r_s
Inside the shell between basic triangular prism and extended triangular prism	R2x	Semicylinder, distance to the edge of the triangular element is less than r_s
	R3x	Outside R2x, distance to the edge of the triangular element is larger than r_s
	R4x	Hemisphere, with distance to the vertex of the triangular elements less than r_s
	R5x	Outside R4x, distance to the vertex of the triangular element is larger than r_s
Outside the extended prism but inside the finite thin layer	R6x	Distance to the edge of the triangular element is larger than r_s
Outside the finite thin layer	R7	Distance to the triangular element is larger than r_s

Note: where x can take 0, 1, or 2 that represent the three edges or vertexes of the triangular element shown in Fig. 6.

Edges and corners are classified for further processing. The projection vector $\boldsymbol{x}_{\mathrm{c(new)}}$ of $\boldsymbol{v}_{\mathrm{xc}}$ on the corresponding edge of the sub-region is calculated by Eq. (15), and the relative vector $\boldsymbol{v}_{\mathrm{xc(new)}}$ is calculated by Eq. (16). The distance t_{nl} between the center of the molecule and the projection $\boldsymbol{x}_{\mathrm{c(new)}}$ is calculated by Eq. (17).

$$\boldsymbol{x}_{\mathrm{C(new)}} = \boldsymbol{x}_{\mathrm{C}} - \left[\frac{1}{b_{\mathrm{i}}|\boldsymbol{v}_{\mathrm{xC}}|}\boldsymbol{o}^{i}_{\mathrm{gK}}\right] \tag{15}$$

$$\boldsymbol{v}_{\mathrm{xC(new)}} = \boldsymbol{x}_{\mathrm{C(new)}} - \boldsymbol{c}_{\mathrm{K}} \tag{16}$$

$$t_{nl} = |\boldsymbol{x}_{\mathrm{C(new)}} - \boldsymbol{x}_{\mathrm{S}}| \tag{17}$$

If $t_{nl} > r_{\mathrm{s}}$, the molecule is located in the sub-region R3x, indicating no overlap with the triangular element.

The projection of $\boldsymbol{v}_{\mathrm{xc(new)}}$ on the adjacent two normal vectors $\boldsymbol{o}_{\mathrm{gk}}$ were calculated by Eqs. (18) and (19) to determine whether the molecule locates in the sub-region R2x.

$$\boldsymbol{p}^{i-1}_{\mathrm{xC}} = \left[\boldsymbol{v}_{\mathrm{xC(new)}}\left(\boldsymbol{o}^{i-1}_{\mathrm{gK}}\right)^{O}\right]\left(\boldsymbol{o}^{i-1}_{\mathrm{gK}}\right)^{O} \tag{18}$$

$$\boldsymbol{p}^{i+1}_{\mathrm{xC}} = \left[\boldsymbol{v}_{\mathrm{xC(new)}}\left(\boldsymbol{o}^{i+1}_{\mathrm{gK}}\right)^{O}\right]\left(\boldsymbol{o}^{i+1}_{\mathrm{gK}}\right)^{O} \tag{19}$$

If Eq. (20) is satisfied, the molecule locates in the sub-region R2x and overlaps with the triangular element.

$$\left|\boldsymbol{p}^{i-1}_{\mathrm{xC}}\right| \le \left|\boldsymbol{o}^{i-1}_{\mathrm{gK}}\right| \wedge \left|\boldsymbol{p}^{i+1}_{\mathrm{xC}}\right| \le \left|\boldsymbol{o}^{i+1}_{\mathrm{gK}}\right| \tag{20}$$

Finally, the distance between the molecule and the adjacent two vertices is calculated. If it is less than r_{s}, the molecule locates in the sub-region R4x, and overlaps with the triangular element. Otherwise, the molecule locates in the sub-region R5x and does not overlap with the triangular element. The Maxwell gas-wall interaction model was employed to update the molecule velocity upon collision, whereas the molecule retained its original motion trajectory in the absence of a collision.

2.2.3. Molecule collides with triangular elements in HS region

In the HS region, where an event-driven scheme is adopted, it is necessary to check whether a molecule will collide with a triangular element in the future. The subparts are checked sequentially by moving the molecule through each one. Once a collision with the triangular element is detected, the corresponding collision time is calculated. The collisions between molecules with surface/edges/vertexes of triangle element are all checked by solving the quadratic equation with time and the presence of positive root means the occurrence of the collision. The algorithm flow chart is shown in Fig. 7, and the corresponding pseudo code is shown in Sec. S1 of the supplementary material.

If the molecule locates in R7 which is outside the surface (Fig. 6a), the time for molecule collides with the surface need to be calculated. The collision time refers to the duration required for the molecule to reach the position where the distance to the basic triangular element surface is r_s. The minimum positive root from the simultaneous equation (Eq. (22)) of the equation for triangular elements surface (Eq. (21)) and the motion equations gives the collision time.

$$Ax + By + Cz + D = 0 \tag{21}$$

$$\begin{cases} at^2 + bt + c = 0 \\ a = \left(Av_x + Bv_y + Cv_z\right)^2 \\ b = 2\left(Av_x + Bv_y + Cv_z\right)\left(Ax_0 + By_0 + Cz_0 + D\right) \\ c = \left(Ax_0 + By_0 + Cz_0 + D\right)^2 - r_{\mathrm{S}}^2\left(A^2 + B^2 + C^2\right) \end{cases} \tag{22}$$

If the molecule locates in the subparts outside the edge (R6x or R3x), the molecules need to be moved to the position that the distance to the edges of the basic triangular element is r_s. The coordination of the start point of the edge is set to be L_0 (l_a, l_b, l_c) and the direction vector is $\boldsymbol{s}$= (m, n, p). The collision time is then calculated by solving the simultaneous equation between motion equation of molecules with the edge (Eq. (23)).

If the molecule locates in the subparts in the corner of extended triangular prism (R5x), the molecule needs to be moved to the position that the distance to the corners of the basic triangular element is r_s. The time for the molecule collides with corner is then predicted in the same way as predicting that of collision between two molecules.

$$\begin{cases} at^2 + bt + c = 0 \\ a = {S_O}^2 + {S_Q}^2 + {S_S}^2 \\ b = 2(S_O S_P + S_Q S_R + S_S S_U) \\ c = {S_P}^2 + {S_R}^2 + {S_U}^2 - s^2 r_{\mathrm{S}}^2 \\ S_O = nv_z - pv_y \\ S_P = n(z_0 - l_c) - p(y_0 - l_b) \\ S_Q = pv_x - mv_z \\ S_R = p(x_0 - l_a) - m(z_0 - l_c) \\ S_S = mv_y - nv_x \\ S_U = m(y_0 - l_b) - n(x_0 - l_a) \end{cases} \tag{23}$$

If the molecule locates inside the basic triangular prism (R1), in the semicylinder (R2x), or in the hemisphere (R4x), the distance between the molecule and the basic triangular is less than r_s, which means that the molecule collides with the triangular element.

2.3. Platform and simulation settings

2.3.1. Simulation platform

The simulations in this work were performed on the Mole-8.5 E platform using 2-socket Linux servers with 2 CPUs of Intel Xeon E5-2680 v2, and the specific software and hardware configuration of the server node is summarized in Table 2.

2.3.2. Simulation settings

Simulations of uniform flow, flow around a cone and IRVE were conducted to validate the boundary conditions and the description of complex walls by triangular elements method, as experimental data are available for comparison. All these three simulations employed

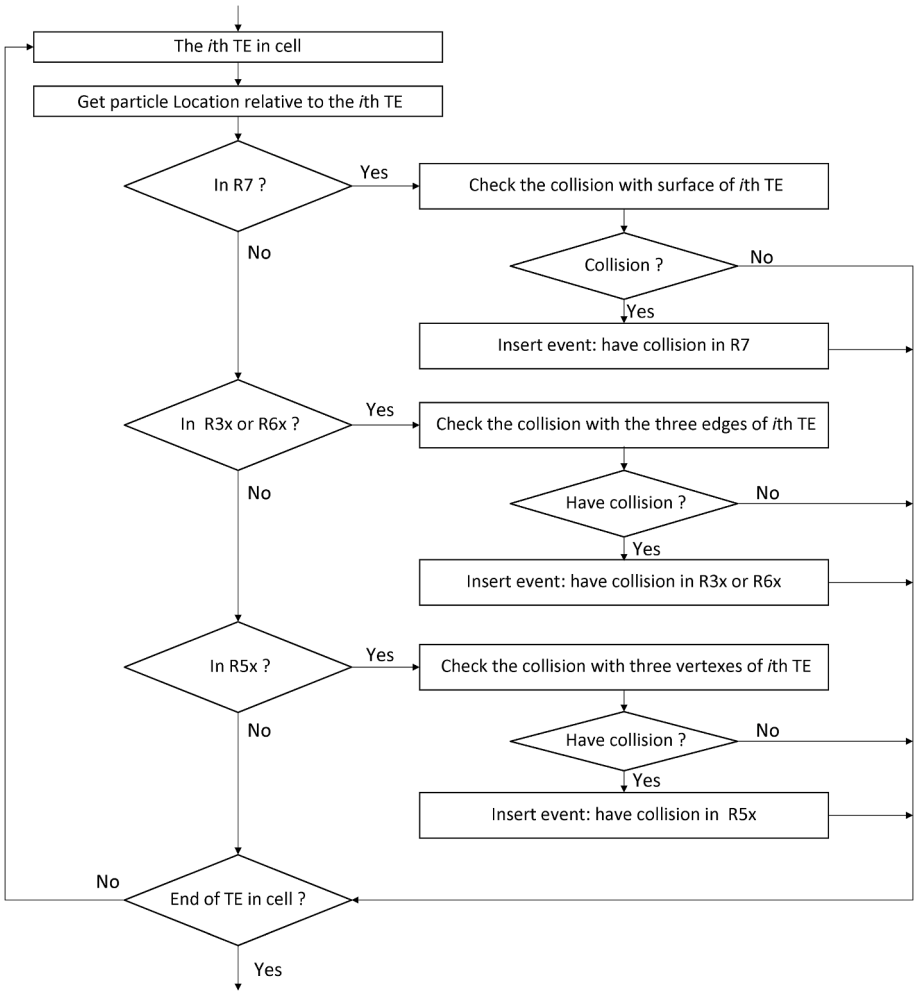

Fig. 7. Algorithm flow chart for checking the collisions between molecules and triangular elements in the HS region. TE is the abbreviation for triangular element.

Table 2
The computation platform and software configurations.

Item	Detail
Platform	Mole-8.5 E
CPUs	Intel Xeon E5-2680 v2 (2.80 GHz, 10 cores)
Host Memory	64 GB DDR3 1333 MHz
OS	CentOS release 6.3 (Final) Kernel:2.6.32-279.el6
Compiler	GCC:4.4.6 Intel compiler:14.0.0

dimensionless numbers, using molecular mass, HS diameter, and time step to normalize other parameters. The simulation of flow around a porous particle in rarefied gases were further carried out. Initially, the molecules were uniformly distributed within a cubic simulation domain, and their velocities were assigned as the sum of a thermal velocity (with spherical distribution) and the flow velocity vector.

Uniform flow field. Uniform flow in the SR without obstacles was simulated using the boundary settings described in section 2.1 and compared with the traditional boundary conditions. The simulation parameters are listed in Table 3 and the translational velocity was adjusted to reach the *Ma* of 0.0 and 13.0. $Ma = 0.0$ means that the translational velocity was set at zero and the flow was driven by thermal diffusion. PID control was added at the CR to regulate the molecular density at the outlet. The pressure, temperature, and velocity distribution along the flow direction calculated from different boundary conditions were compared. The molecular volume fraction η in the SR was calculated and compared with the preset molecular volume fraction η_{set}.

The translational velocity was then adjusted to realize the *Ma* at 0.0, 0.13, 1.3, and 13 respectively to validate the applicability of the boundary conditions at different *Ma*. The length-to-diameter ratio of the SR L_x/L_y was changed at different *Ma* and the molecular volume fraction at steady-state conditions were calculated and compared with the preset molecular volume fraction.

Flow around non-spherical objects. To demonstrate the adaptability of this approach in geometrically complex objects, high *Ma* flows around a conical particle and an IRVE were then simulated. The geometry ratio of the simulation zone was set to 15*D*: 20*D*: 20*D* (*D* is the characteristic length of the system, where for a cone it is taken as the base diameter) to eliminate the influence of obstacles on the flow field (Zhang et al., 2016b), and the parameter independence tests for domain width are presented in Fig. S2 of the supplementary material. The *x*-axis was defined as the flow direction. The completely decoupled inlet-outlet

Table 3
Parameters for simulation of uniform flow.

Number of molecules, N	Volume fraction, η	Mass, m	HS diameter, d_{HS}	PP diameter, d_{PP}	Temp., k_BT	Velocity, v	PP time step, Δt
$50 \times 50 \times 50$	0.0082	1.0	1.0	1.008	8.33×10^{-4}	0.0	1.0

boundary conditions with PID control were applied at x-direction. Non-periodic boundary conditions were used in y- and z-directions. Triangular elements method was used to approximate the wall of the static bodies.

(1) Flow around a conical particle

The discrete triangular elements were used to resolve the cone wall and compared with the analytically derived model. The ratio of wall temperature T_w and the flow temperature at infinite distance T_0 was set at 0.01, 0.1, and 1. The thermal accommodation coefficient α was changed in the range of 0.7–1.0 to find the appropriate simulating temperature at which the calculated drag coefficient changes monotonically with α. Additional simulation parameters are listed in Table 4.

The drag coefficients at different Kn (Keel et al., 1972) were calculated at the chosen temperatures under complete and partial diffuse reflection conditions (α set to 1 and 0.4) respectively. The Ma was maintained at 7.6 and the remaining simulation parameters are provided in Table 5.

(2) IRVE in rarefied gas

The cone in Fig. 4 was replaced with the IRVE. The aerodynamics were simulated by HS-PPM and DSMC, respectively. DSMC simulations were carried out using the SPARTA software (version 18Jul 2022) (Plimpton et al., 2019). The literature (Moss et al., 2006) found drag coefficients were calculated by SPARTA based on same parameters including Larsen-Borgnakke statistical energy model and variable hard sphere molecular model to validate the accuracy of SPARTA. HS model was further used in DSMC simulation to validate the applicability of HS-PPM in simulating IRVE under rarefied conditions. The drag coefficients calculated from the above two methods were compared. The simulation parameters are listed in Table 6.

(3) Flow around a porous particle

The structure of the porous catalyst (for demonstration tests, regardless of the catalyst types) was utilized. It has an average solid volume fraction of 72.05%, from which the spherical particles of 1–3 μm were randomly selected for flow simulations. Specifically, the flow around a spherical porous particle with a diameter of 2 μm was simulated and the detailed characteristics of the flow field were presented. The simulation parameters are listed in Table 7.

3. Results and discussions

The uniform flow simulation (Section 3.1) serves to validate the new inlet/outlet boundary conditions with PID control, as there is no solid wall. The cone flow (Section 3.2.1) validates the triangular element wall method together with the new boundary conditions by comparing with analytical wall treatment and experimental drag coefficients. The IRVE simulation (Section 3.2.2) also validates the combined framework for a realistic complex geometry against DSMC results. The porous particle simulation (Section 3.3) is presented as a demonstration of capability, not a formal validation.

3.1. Performance of boundary conditions in uniform flow

Uniform flow simulations were conducted using four boundary condition schemes: the zero gradient boundary conditions with PID control proposed in this work, the traditional free stream inlet/outlet conditions (Zhang et al., 2016), the implicit boundary conditions without adding collision (Akkaya et al., 2015), and the implicit boundary conditions with adding collisions (Akkaya + Coll). The introduction of PID control does not compromise simulation efficiency compared to other boundary settings.

The boundary conditions proposed in this work require the proportional, integral, and derivative coefficients of the PID controller. Fig. 8 (a) shows an example for tuning the PID coefficients at $Ma = 0.13$. The three PID coefficients were first set to −1, −1, and −1, and the volume fraction fluctuations around the preset value were simulated. Owing to low-frequency, large-amplitude oscillations of the volume fraction, it is necessary to increase the integral coefficient and reduce the derivative coefficient. It can be seen that with parameter tuning, the volume fraction of the system gradually approaches the preset value (red dashed line) and stabilized when the parameters were set to −1, −10, and 0. Subsequently, each parameter was individually varied by 10% and 20% to check the sensitivity of the parameters in Fig. 8(b). It shows that a 20% variation leads to considerable fluctuations, yet the volume fraction (single time step, without time-averaged) still remained within 1.3% of the preset value. This indicates that the results from this work are not sensitive to the small variation of the chosen PID coefficients.

Fig. 9 shows that, unlike the traditional free stream inlet/outlet condition, both the present method and the implicit boundary conditions successfully achieved a uniform translational velocity (Fig. 9c and d) along the flow direction without significant pressure difference (Fig. 9a and b). The discrepancy of the fluctuations of temperature (Fig. 10a and b) and molecular volume fraction η_{fluc} (Fig. 10c and d) along the flow direction predicted by the improved model presented in this work are also similar to that from the implicit boundary conditions, suggesting that the developed boundary settings with PID control achieve reasonable flow field in the uniform flow situation. The traditional free stream inlet/outlet boundary conditions lead to significant disturbances in pressure, velocity, temperature, as well as molecular volume fraction due to the coupling between the inlet and outlet (Figs. 9 and 10).

The influence of coupling between inlet and outlet gets more significant under low Ma conditions indicated by the clear fluctuations in Figs. 9(a) and 10(a, c). At low Ma condition (Fig. 10c), the molecular volume fraction η from this work and the implicit boundary conditions with adding collisions (Akkaya + Coll) fit the preset values well along the flow direction. While the implicit boundary conditions without adding collisions (Akkaya et al., 2015) result in lower η, and the traditional free stream inlet/outlet conditions (Zhang et al., 2016) present apparent fluctuations at both the inlet and outlet due to lack of molecular balance. The differences among the four boundary conditions decrease at high Ma (Figs. 9b and 10b and d) since the flow field at high Ma is dominated by the translational velocity. Further tests of the boundary settings developed in this work as varying the length to diameter ratios from 0.5 to 8 show that the deviation of the calculated molecular fraction in the SR from the preset values are within ±1% (Fig. 11), suggesting that this newly developed boundary conditions could realize reasonable flow field at wide Ma ranges. Fig. 11 also shows that the deviation from preset value gets less significant at higher Ma conditions.

Above comparison shows that the boundary settings proposed in this work are capable to provide reasonable density, temperature, pressure, as well as velocity fields in uniform flow at both low and high Ma conditions. The periodic boundary conditions can generally provide stable flow properties but significant fluctuations occur in free stream

Table 4
Parameters for simulation of flow around a cone under cold wall surface.

Knudsen number, Kn	Reynolds number, Re	Half cone angle, θ	Base diameter, D	HS diameter, d_{HS}	Temperature ratio, T_w/T_0	Volume fraction, η	Velocity, v
0.278	126	10°	7.448	1.0	0.010	0.050	0.400

Table 5
Parameters for simulation of the flow around a cone under isothermal wall conditions.

Knudsen number, *Kn*	Reynolds number, *Re*	Half cone angle, θ	Base diameter, *D*	HS diameter, d_{HS}	Volume fraction, η	Velocity, *v*
1.0	11.33	9°	4.38	1.0	0.02534	0.1155
0.8	14.16	9°	5.49	1.0	0.02529	0.1154
0.6	18.88	9°	7.37	1.0	0.02519	0.1154
0.4	28.32	9°	10.98	1.0	0.02534	0.1154
0.2	56.65	9°	21.39	1.0	0.02597	0.1157

Table 6
Parameters for simulation of the IRVE.

Altitude (km)	Knudsen number, *Kn*	Reynolds number, *Re*	Mach number, *Ma*	Base diameter, *D*	Temp., k_BT_0	Volume fraction, η	Velocity, *v*
125	1.74	1.81	1.98	20.0	1.33×10^{-4}	3.35×10^{-3}	0.0299
120	1.064	3.35	2.24	40.0	1.33×10^{-4}	2.78×10^{-3}	0.0338
115	0.574	7.16	2.58	40.0	1.33×10^{-4}	5.08×10^{-3}	0.0392
110	0.257	18.9	3.06	100.0	1.33×10^{-4}	4.53×10^{-3}	0.0464
105	0.103	53.9	3.49	100.0	1.33×10^{-4}	1.11×10^{-2}	0.0544

Table 7
Parameters for simulation of flow around a porous particle.

Sim. Domain	Volume fraction, η	HS diam., d_{HS}	Temp., T_0	Velocity, *v*	PP time step, Δt	Sim. Duration
4μm × 6μm×6 μm	8.18×10^{-6}	10 Å	1123 K	100 m/s	10 fs	40 ns

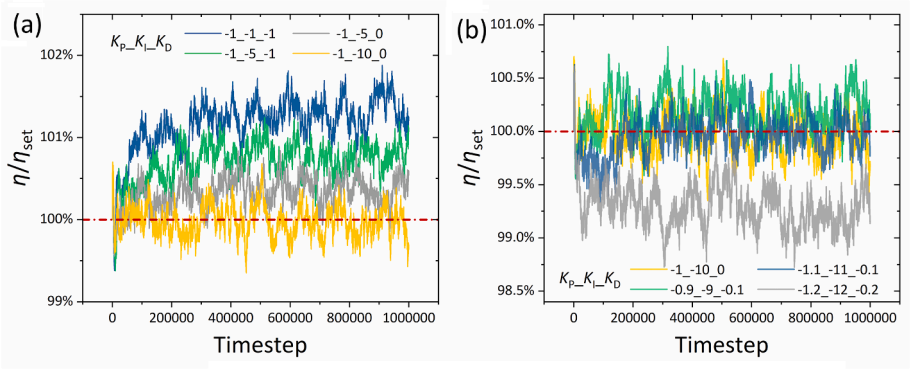

Fig. 8. Tuning process and sensitivity analysis of PID coefficients (*Ma* = 0.13). (a) Adjustment of the proportional, integral, and derivative coefficients of PID controller in the boundary conditions; (b) Sensitivity analysis about the influence of the PID coefficients on stability.

inlet/outlet condition where the decoupling of inlet and outlet is essential (Zhang et al. in Figs. 9 and 10). While traditional implicit boundary conditions can be used with specified outlet properties, their applicability is restricted to the idealized scenario of uniform flow. In practical applications, the characteristics of the outlet flow field remain entirely unclear, revealing a key limitation of traditional implicit boundary methods. The boundary settings proposed in this work possess the advantage of implicit boundary conditions that avoid the instability at both the inlet and outlet. On this basis, molecular collisions were introduced at both ends to regulate pressure balance, and PID control was supplemented to mitigate the outlet fluctuations. This combined approach successfully generated a uniform flow, characterized by a pressure-independent translational velocity and negligible streamwise gradients in temperature and number density. These results indicate that the newly developed boundary conditions are capable of providing reasonable flow field for uniform flows and can be used in more realistic situations with unknown outlet properties.

3.2. Validation of combined framework

The boundary conditions developed above and the introduction of triangular elements enabled HS-PPM to simulate more complex multiphase systems. We simulated high Knudsen number flow from two distinct perspectives: flow around supersonic flying objects and porous nano particles. While the latter was directly simulated to reproduce the real flow field from an atomic level, the former was scaled down by maintaining the same dimensionless numbers, *Re*, *Kn*, and *Ma*, for the simulations and experiments, so as to reduce computational cost.

Owing to the lack of nano/micro-scale experimental data for direct comparison, we validated the improved model against macro-scale experimental data at the same dimensionless numbers, specifically for flow around a conical particle and IRVE.

3.2.1. Simulation of flow around a conical particle

Simulation of the flow around a conical particle was carried out and the cone surface was described by both analytically derived model and the discrete triangular elements method developed in this work. A systematic comparison was conducted between simulation and benchmark experimental results. Cold wall condition was widely adopted in the supersonic speed wind tunnel experiments under rarefied flows (Bailey & Hiatt, 1972; Keel et al., 1972; Moss et al., 2006; Voronin & Zhdanova, 1987; Yamamoto et al., 2006). Generally, the thermal accommodation coefficients are assigned boundary values of 0 and 1 to establish theoretical extremes in simulations, and the rationality is confirmed if the

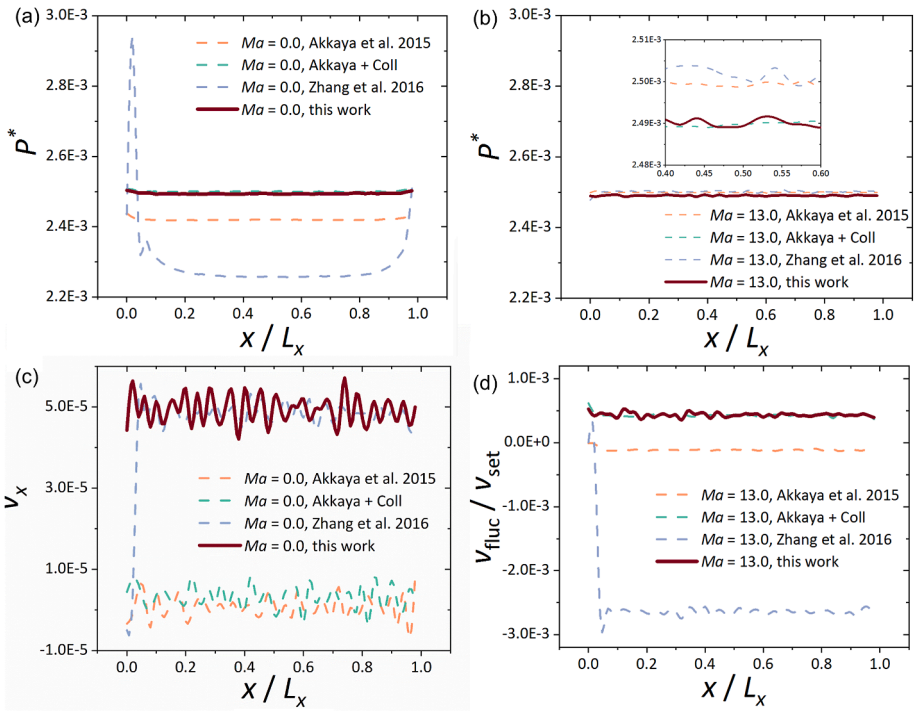

Fig. 9. Comparison of average pressure and molecular velocity along the flow direction at $Ma = 0.0$ and $Ma = 13.0$ calculated from different boundary conditions. (a) Pressure, $Ma = 0.0$; (b) pressure, $Ma = 13.0$; (c) velocity, $Ma = 0.0$; (d) velocity, $Ma = 13.0$. For easier comparison, the variation in velocity at $Ma = 13.0$ is shown in the fluctuation relative to the preset velocity. $Ma = 0.0$ means that the translational velocity was set at zero and the flow was driven by thermal diffusion.

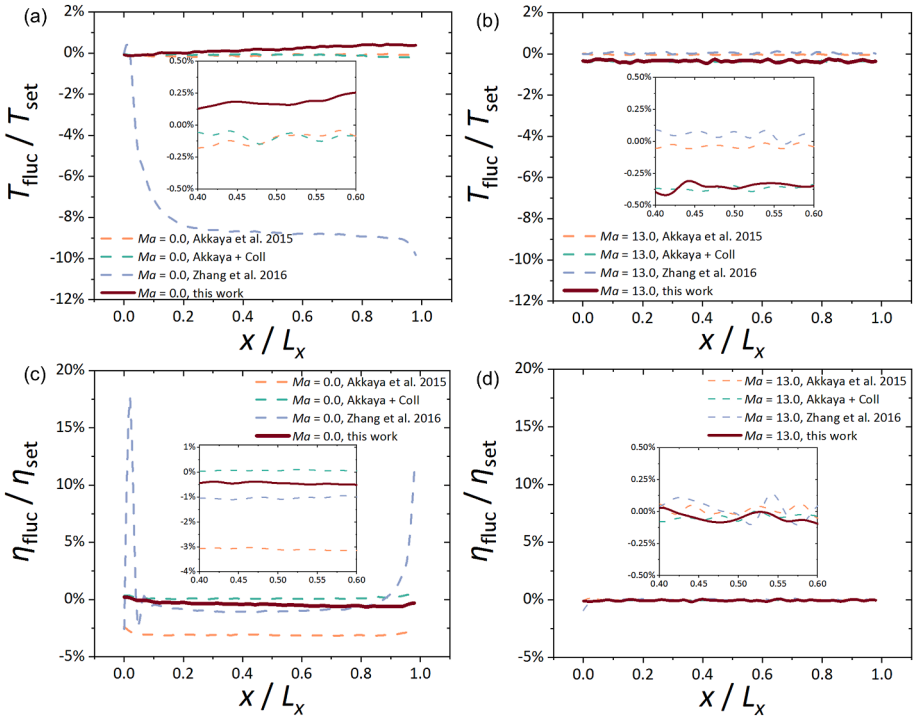

Fig. 10. Comparison of temperature and molecular volume fraction fluctuations around the preset value along the flow direction at $Ma = 0.0$ and $Ma = 13.0$. (a) Temperature, $Ma = 0.0$; (b) temperature, $Ma = 13.0$; (c) molecular volume fraction, $Ma = 0.0$; (d) molecular volume fraction, $Ma = 13.0$. $Ma = 0.0$ means that the translational velocity was set at zero and the flow was driven by thermal diffusion.

drag coefficient measured in experiment fall within this simulation range. However, Fig. 12 shows that the drag coefficient does not always change monotonically with the thermal accommodation coefficient and the trend depends on the ratio of wall temperature relative to the free stream (T_w/T_0). At $T_w/T_0 = 0.01$, the drag coefficient initially increases with the thermal accommodation coefficient in the range of 0.7 to 0.9, and subsequently decreases as the thermal accommodation coefficient is further increased. At higher wall temperatures, the relationship between

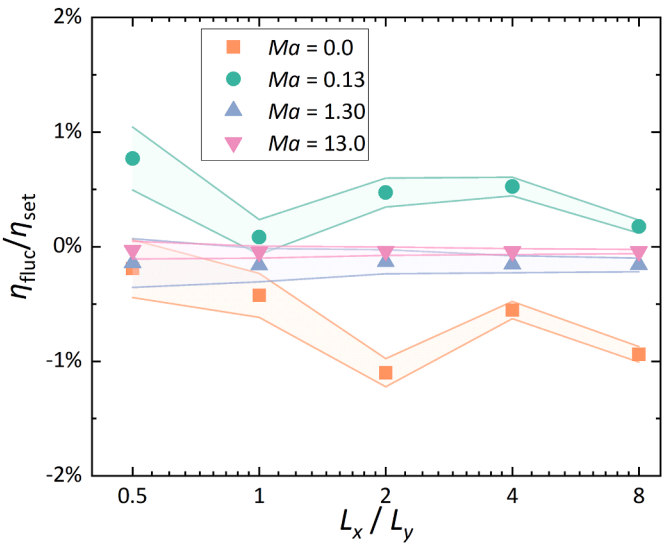

Fig. 11. Variation of η under different L_x/L_y ratios at Ma equals to 0.0, 0.13, 1.3, and 13.0. The shadows in the figure represent the fluctuation range (min-max) of molecular volume fraction. $Ma = 0.0$ means that the translational velocity was set at zero and the flow was driven by thermal diffusion.

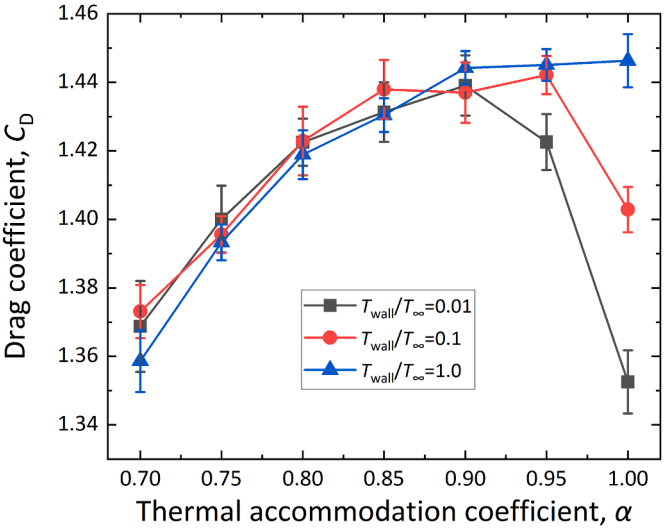

Fig. 12. Drag coefficient at different thermal accommodation coefficient and wall temperature ($Kn = 0.278$, $Ma = 24$).

drag coefficient and thermal accommodation coefficient gradually changes to a monotonic trend. At $T_w/T_0 = 1$, the maximum drag coefficient was achieved at the complete diffuse reflection condition where the thermal accommodation coefficient equals to unity (Fig. 12). This finding indicates that assuming thermal accommodation coefficients of 0 or 1 fails to encompass the full range of possible drag coefficients, leading to discrepancies between simulation and experiment. Consequently, the influence of wall temperature must be considered.

It is widely accepted that the drag coefficient is presented as a function of the Kn when the rarefaction effect is involved (Figliola et al., 2022; Mailler et al., 2023; Tao et al., 2017; Tao & Guo, 2017). The wind tunnel experiments at high Ma and transition flow (Kn in the range of 0.1–1) conditions was carried out by Keel et al. (1972) and the experimental found drag coefficients of nitrogen flow around a conical particle are represented by the black line in Fig. 13.

Fig. 13 shows the drag coefficients from HS-PPM and DSMC (the parameter independence tests are presented in Fig. S1 of the

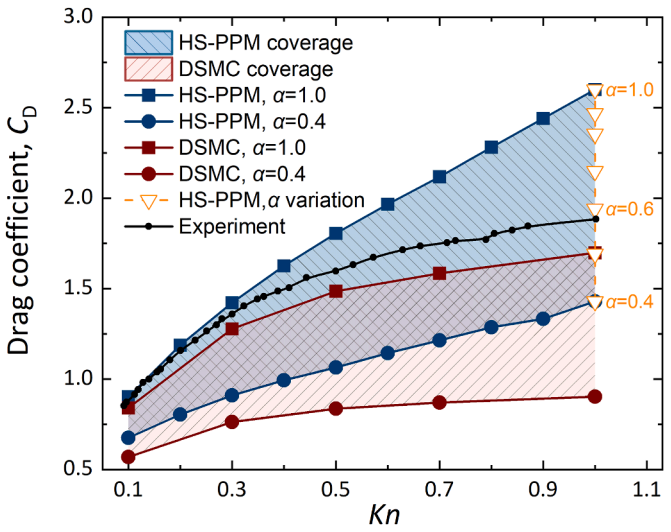

Fig. 13. Comparison of drag coefficients from simulations and wind tunnel experiments. Experiments (black line), HS-PPM (blue line and region), and DSMC (red line and region) at complete diffuse reflection condition ($\alpha = 1$) (square symbols) and partial diffuse reflection condition ($\alpha = 0.4$) (circle symbols) in the transition flow range ($Kn = 0.1$–1). The wall temperature for the experiments and simulations was equal to the free stream. The statistical errors across all groups were maintained below 1.1%.

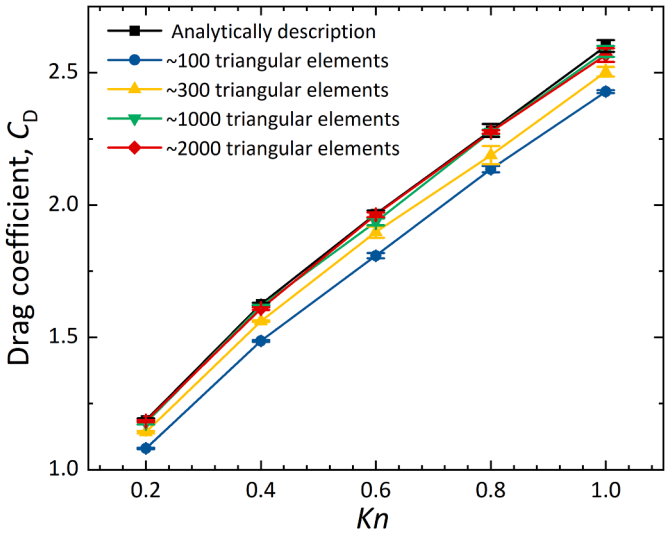

Fig. 14. Comparison of drag coefficients using both analytically description and the triangular elements description.

supplementary material) at both partly diffuse reflection ($\alpha = 0.4$) and complete diffuse reflection ($\alpha = 1$) conditions in the transition flow range ($Kn = 0.1$–1). For HS-PPM, the experimental found drag coefficients show close agreement with the simulation results at $\alpha = 1$ at low Kn conditions ($Kn = 0.1$–0.4), indicating the complete diffuse reflection collision between molecule and wall. As further increasing the Kn, the fraction of specular reflection increases and the experimental value locates between the $\alpha = 1$ and $\alpha = 0$. The drag coefficient at varied thermal accommodation coefficient in the range of 0.4–1 with an increment of 0.1 was simulated at $Kn = 1$, and the experimental found drag coefficient fit the $\alpha = 0.6$ was observed. Fig. 13 also proves the experimental values fall entirely within the parameter range of HS-PPM (blue region); however, for DSMC, the maximum drag coefficients (red region) are still lower than those observed in experiments (perhaps owing to the relatively high density of the gas employed in this experiment), further demonstrating the superior accuracy of HS-PPM.

The resolution of triangular elements method was tested by comparing the drag coefficients in flow around a cone at the same condition using both analytically description and the triangular elements description with the number of facet varied in 100–2000 (Fig. 14). It can be seen that when the number of triangular element is approximately 100, the drag coefficients from the triangular elements method are always lower than that from the analytical derivation of cone. The discrepancy gradually decreases with increasing the number of triangular element, and the difference is negligible when the number of facet exceeds 1000. This suggests that triangular elements method with sufficient number of facet can provide equal-level resolution as the analytically method.

The efficiency of the analytical model and triangular elements methods was evaluated at varied thermal velocity conditions. The simulation parameters are listed in Table S2, and the number of collisions and computing time for gas phase flow without and with cone described by analytically resolved model and triangular elements method were presented in Fig. 15. For easier comparison, single-process simulations were carried out in these three cases and the collision number and time cost in 2000 steps were averaged after running for 10,000 steps and reaching steady state. The size of the cone is negligible and its impact on gas collision can be neglected, hence only the number of collisions and time costs for gas collisions in uniform flow simulation are shown for comparison (yellow in Fig. 15). It is found that the triangular elements method increases the per-step computational cost by a factor of ~1.25 relative to the analytical wall description for the cone geometry. Nevertheless, its key advantage is universal applicability to arbitrarily complex surfaces where analytical description is impossible. Therefore, the improvement in "efficiency" refers to geometric versatility rather than the absolute speed only. Further combination of the analytical method and triangular elements method in the future offers a fresh approach to balance the accuracy and efficiency and realize versatile simulation of complex solid particles.

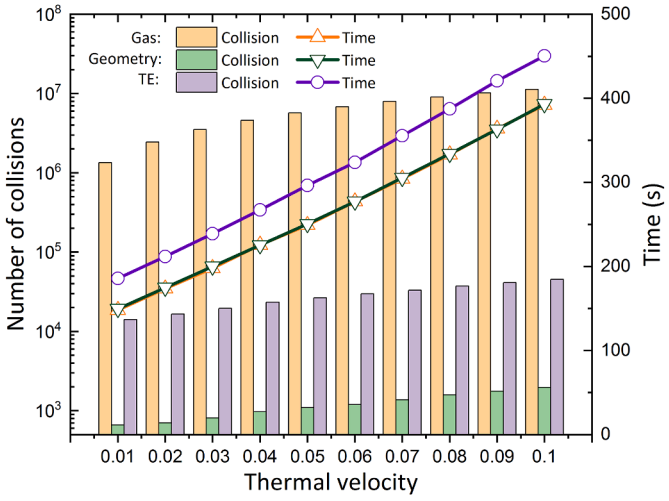

Fig. 15. Performance of flow around cone using analytically resolved model and triangular elements method at different thermal velocities. The scatters with solid lines represent the time needed to calculate the collisions between gas particles (orange), between gas particles and cone surface in geometric method (green), and between gas particles and cone surface in triangular elements method (purple). The columns show the number of collisions and the colors are assigned in the same way as the time.

3.2.2. IRVE in rarefied gas

Simulations on the basis of exactly the same flow are limited by the computational costs, whereas the dimensionless numbers enable the modeling of larger systems with relatively lower costs. Based on the same *Re*, *Kn*, and *Ma*, the fly of the reentry vehicle at 110 km height was scaled and simulated using HS-PPM with developed boundary conditions and triangular elements method to describe the surface of the reentry vehicle (Fig. 16a). The temperature field and flow field in Figs. 16 and 17 show obvious shock wave characteristics, indicating that the high speed gases deflect along the cone surface of the inflatable bladder of IRVE. The thickness of the shockwaves is in similar dimension with the bladder (Fig. 16). In the areas close to the vertex of the inflatable bladder, temperature and density suddenly change to more than three times of the free stream (Fig. 16b). However, the temperature and flow density around the centerbody structure remain consistent with those in the free stream (Figs. 16b and 17b), suggesting that the inflatable bladder could effectively protect the centerbody structure of the IRVE. Benefiting from the sheltering effect of the inflatable bladder, the number density on the leeward keeps low (Fig. 17b) but the temperature is 2–3 times of the free stream temperature (Fig. 16b), suggesting that the length of the centerbody can be further adjusted to avoid the high temperature effects.

The distributions of molecular volume fraction η, temperature T, and heat flux J along the central axis in the flow direction are presented in Fig. S3 of the supplementary material. Both distributions are normalized by the free stream for better comparison. The stagnation point locations

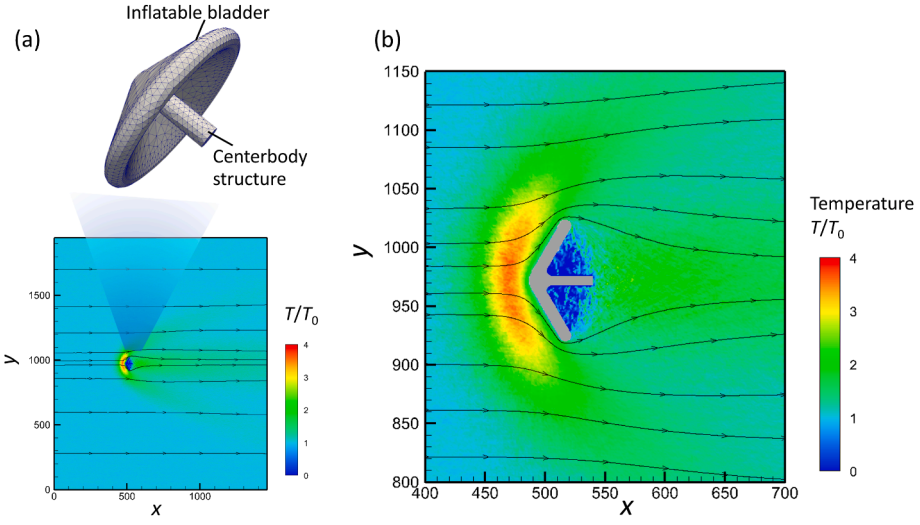

Fig. 16. Temperature distribution of reentry vehicle simulated by HS-PPM. (a) temperature field around the reentry vehicle with the details of the structure; (b) the magnification of the temperature field near reentry vehicle.

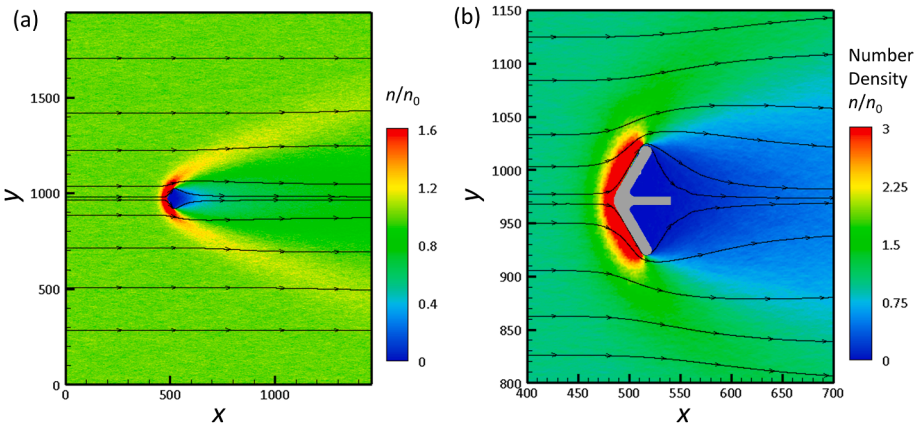

Fig. 17. Density distribution of reentry vehicle simulated by HS-PPM. (b) is the magnification of the temperature field near the reentry vehicle in (a). The number density is shown in dimensionless number relative to the density of the free stream.

for density and temperature are inconsistent, whereas the minimum point of the heat flux curve aligns with the temperature, and the maximum corresponds to the density. The J/J_0 of DSMC at 110 km is 8.37 (Moss et al., 2006), which is comparable with our results. Although it is widely accepted that the drag coefficient can be directly compared under identical *Re*, *Kn*, and *Ma* conditions, a precise comparison of flow field profiles—such as heat flux, density, or temperature—requires the introduction of additional dimensionless numbers, which are not considered in this work yet. This necessity may explain the discrepancy arising in heat flux.

The drag coefficients calculated by HS-PPM and DSMC at different flight altitudes (corresponding to different *Kn*) are compared and shown in Fig. 18. DSMC simulations carried out in this work using SPARTA (Plimpton et al., 2019) perfectly reproduced the drag coefficients from literature based on the Larsen-Borgnakke energy model and variable hard sphere model (Fig. 18a). Fig. 18(b) shows that the drag coefficients from HS-PPM and DSMC are close when $0.1 < Kn < 1$ (where the relative error remained below 1.8% throughout the 105–120 km altitude range), indicating the consistency between improved HS-PPM and DSMC in transitional flow where the drag coefficient still depends on *Re*, *Kn*, and *Ma*, implying the continuum hypothesis. Thus, the optimized HS-PPM was validated and demonstrated acceptable accuracy for investigating rarefied gas flow aerodynamics.

As altitude increases and $Kn > 1$, the flow shifts to the free molecular flow regime where continuum-based traditional fluid mechanics methods gradually fails. Although trillion-scale MD is already possible, it is still far behind the requirement for direct MD simulation of IRVE by several orders of magnitudes. HS-PPM is therefore limited to the low *Kn* conditions where the dimensionless-number-based scaling law is reasonable. However, HS-PPM can be used in combination with DSMC in a manner that HS-PPM provides accurate flow field near the wall while DSMC simulates the bulk gas flow. The boundary settings proposed in this work can be used for the transition between HS-PPM and DSMC, while the next section will demonstrate the ability of HS-PPM in the simulations of complex walls such as porous particles. This unfolds a fresh perspective in balancing the overall efficiency and the accuracy of detailed characteristics such as shocks waves close to the aircrafts, and could apparently support the development and optimization of aircraft in the aerospace field.

3.3. Applications: flow around a porous particle

The improved model was subsequently extended to simulate the flow past porous nano-particles which have more complex hierarchical structures. It should be noted that the simulations of porous particle are used solely for demonstration the capability of the improved HS-PPM rather than a fully validated results, and the current model can be universally applied to transport phenomena (including flow, diffusion, and heat transfer) in similar nano/microscale complex structures. The gas flow around a spherical porous particle with a diameter of $D = 2$ μm was simulated under nano/micro flow conditions, as shown in Fig. 19. The radius of the gas molecules is 5 Å, the size of the simulation domain is 2*D*: 3*D*: 3*D*, the velocity along the flow direction is 100 m/s (this is extremely high for typical nanoflow but possible for some aerospace applications), and the temperatures of the gas and wall are 1123 K, other simulation parameters are listed in Table 7. Fig. 19 shows that under a low flow velocity ($Ma = 0.13$, $Re = 0.03$, and $Kn = 7.20$), the density field in the central cross-section along the *z*-axis is nearly uniform and the flow at both the inlet and outlet are stable.

Furthermore, the distributions of temperature and number density along the *xy*-plane and *yz*-plane were obtained by slicing through the central planes along the *z*-axis and *x*-axis, respectively. In Fig. S4 of the supplementary material, the blue regions in the nephograms represent the cross-sectional profiles of the porous structures. Analysis of the density field reveals that at a low flow velocity ($Ma = 0.13$), most regions exhibit relatively uniform density. However, the density inside the porous particle shows different trends on the *xy*-plane, the density is approximately 20% higher on the windward, while that is slightly lower on the leeward. This phenomenon is attributed to the resistance encountered by the gases as they traverse the catalyst channels. In contrast, the temperature field is relatively homogeneous, with fluctuations of approximately 10% around the average temperature on both the *xy*-plane and *yz*-plane.

We then varied the particle diameter from 1 μm to 3 μm and quantified the difference in drag coefficients between the spherical porous particles and their spherical analogues. The theory of flow around a sphere is well-established: the drag coefficient follows Stokes' law for $Kn < 0.01$, and becomes independent with *Kn* at high *Kn* values ($Kn > 100$) (Cheng et al., 1988), adhering to the free-molecular limit. However, there is a lack of theoretical formulas for the intermediate Knudsen number range. Consequently, a semi-empirical slip correction factor C_C for the drag coefficient based on the Cunningham framework was introduced (Allen & Raabe, 1985; Sun et al., 2018). Specifically, the drag coefficient is generally determined by the Knudsen-Weber formulation of the slip correction factor, whose general formula is given by Eq. (25). Here in Table 8, we present the parameters of C_C from representative literatures (Allen & Raabe, 1985; Davies, 1945; Sun et al., 2018).

$$C_D = \frac{24}{ReC_c} = \frac{24}{\sqrt{\frac{\pi\gamma}{2}}\frac{Ma}{Kn}C_c} \tag{24}$$

$$C_c = 1 + Kn\left[A_1 + A_2 \exp\left(-\frac{A_3}{Kn}\right)\right] \tag{25}$$

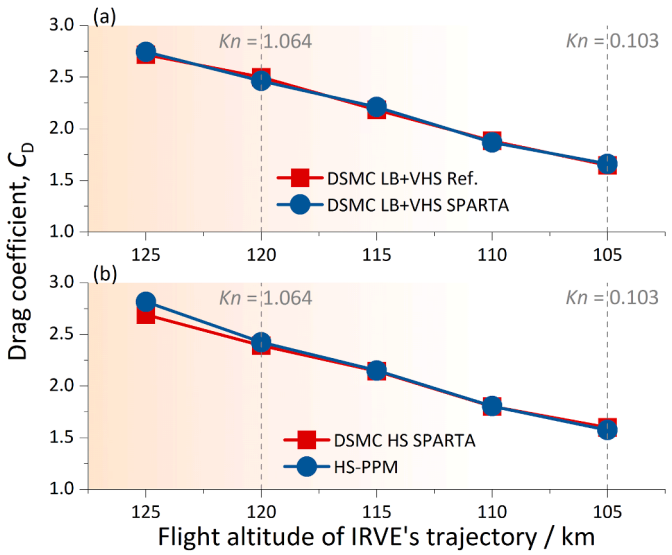

Fig. 18. Drag coefficients simulated by DSMC and HS-PPM at different flight altitudes. (a) Reproduction of the literature found drag coefficient by DSMC using SPARTA software; (b) Comparison between the drag coefficients from DSMC and HS-PPM. The statistical errors across all groups were maintained below 0.5%.

As shown in Fig. 20, while the variation of C_D with *Kn* seems irregular, a distinct linear relationship between C_C and *Kn* emerges after the conversion of C_D to C_C through formula transformation. Therefore, a linear fitting was directly applied, resulting in the relationship: $C_C = 3.493^{*}Kn + 2.102$. The red and black dashed lines in the figure represent the curves of C_C and C_D obtained by applying this fitting formula, which are in good agreement with the original data points.

A final comparison of the drag coefficients for flow around a sphere and a porous particle is presented in Fig. 21. It can be observed that the drag coefficient for the porous particle is significantly reduced due to the introduction of internal channels. Furthermore, the drag coefficient varies unsmoothly with *Kn*, which arises from the random cut of the spherical sub-region from the entire catalyst (the average volume fraction is 72.05%). Unlike the solid spheres, whose drag coefficient increases with *Kn*, porous spheres exhibit an opposite tendency as *Kn* rises. This behavior occurs because an increase in *Kn* corresponds to a reduction in sphere diameter, whereas the pore size distribution remains unchanged. As a result, the ratio of sphere-to-pore diameter gradually decreases. Therefore, it is essential to maintain a fixed ratio of sphere-to-pore diameter for further in-depth analysis.

Table 8
Parameters for Cunningham-based slip correction factors.

Authors	A1	A2	A3
Millikan, 1923	2.418	0.812	0.447
Davies, 1945	2.514	0.800	0.550
Michael et al., 1985	2.284	1.116	0.500
Hutchins et al., 1995	2.462	0.938	0.589
This work	3.493	1.102	0

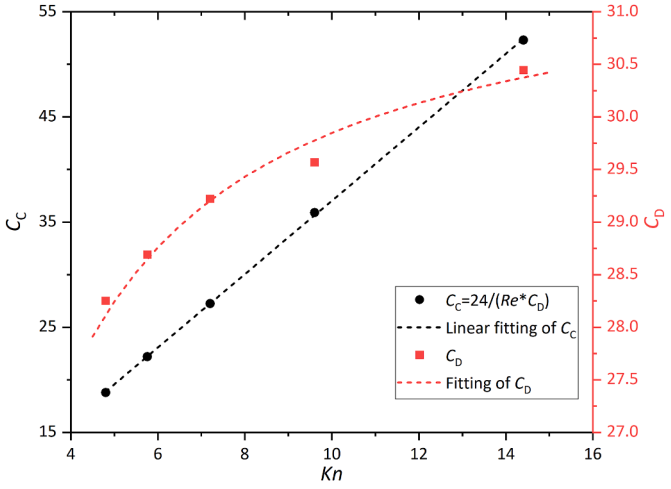

Fig. 20. Variation of drag coefficient and C_C with *Kn* for flow around a sphere.

$$C_{D,\mathrm{limit}} = \frac{e^{-S^2/2}}{\sqrt{\pi}S^3}\left(1+2S^2\right) + \frac{4S^4+4S^2-1}{2S^4}\mathrm{erf}(S) + \frac{2\sqrt{\pi}}{3S_w} \tag{26}$$

$$S = \frac{U}{\sqrt{2RT}} = \sqrt{\frac{\gamma}{2}}Ma \tag{27}$$

The theoretical drag coefficient in the free-molecular limit (i.e., at infinite Knudsen number) for a smooth sphere (Schaaf & Chambré, 1961), given by Eq. (26), was also calculated. As shown in Fig. 21, with decreasing sphere diameter, the drag coefficient for the sphere gradually increases with *Kn* and approaches the theoretical limit, which is consistent with experimental findings. However, a discrepancy exists

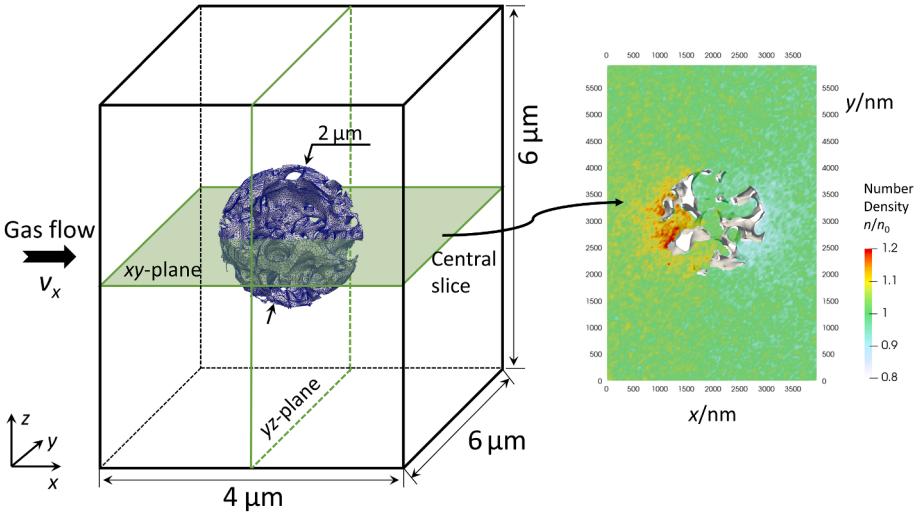

Fig. 19. Simulation setup of the flow around a spherical porous particle and the density field around the *xy*-plane.

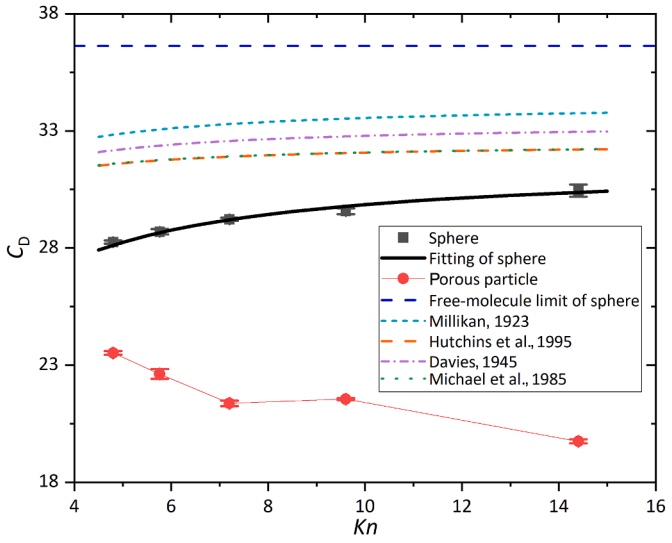

Fig. 21. Comparison of drag coefficients for flow around a sphere and porous particle.

between our fitted limit (31.64) and the theoretical drag (36.63), which is similar to the findings reported in other literatures (Allen & Raabe, 1985; Davies, 1945; Sun et al., 2018) (with extreme values ranging between 32 and 34) as shown in the figure. This can be attributed to two main factors: Firstly, our simulations were conducted within a finite computational domain, whereas the theoretical value is derived for an infinite space. While this spatial blocking effect of boundary walls diminishes with increasing *Kn* and becomes negligible in the free molecular flow (Goswami et al., 2020; Schaaf & Chambré, 1961), the variation in *Kn* across our simulation means that the drags at lower *Kn* are more affected by spatial blocking. This enhancement will lead to a further increase in the slope of the fitting curve, bringing it closer to the theoretical limit. Secondly, due to the limited range of *Kn* investigated, the fitting was performed using a linear function, which fails to capture the exponential term present in the Cunningham-based equation. A more accurate result would require fitting across a broader range of Knudsen numbers.

4. Conclusions

This work achieved net transport of rarefied gas in the absence of a driving pressure gradient in flows over geometrically complex particles and objects. The zero gradient boundary conditions were accomplished through a completely decoupled inlet and outlet as well as a PID control at outlet, and the wall geometry was described by triangular elements to further broaden the applicability of HS-PPM for the realistic multi-phase flow scenarios. The comparison between the zero gradient boundary conditions and the traditional boundary conditions in uniform flow at both high and low *Ma* (0.0–13.0) validated the reliability of the newly developed boundary settings. The accuracy of the triangular elements method was verified by both experiment and simulation results for flow around a conical particle ($Kn = 0.2$–1.0). And the consistence between the drag coefficients from HS-PPM and DSMC of flow around IRVE under rarefied conditions at low *Kn* conditions ($Kn = 0.1$–1.7, transitional flow regime that close to continuum flow regime) also validated the accuracy of the improved HS-PPM models.

The inlet/outlet boundary condition and triangular elements method were further adopted in simulating high *Kn* gas flows such as the flow around a micro-meter-scale porous particle. HS-PPM successfully provided the temperature and density distribution inside the pores as well as around the particle. Compared to a solid spherical particle of identical size, the porous structure lowers the drag coefficient, while the value observed remains within a reasonable range. This suggests that the optimized HS-PPM provides not only detailed mass and heat transfer properties for the flow at micro scale, but also reliable results for simulating the aerodynamics under rarefied conditions based on the dimensionless numbers. It is anticipated that more accurate and efficient simulations can be achieved to support the design and optimization of aircrafts and porous catalysts with the future development in the coupling between HS-PPM and DSMC. In addition, the PID coefficients in zero gradient boundary conditions were manually fine-tuned and their quantitative relationship with operating conditions was not investigated, automatically tuning the PID coefficients is therefore promising in further widening the application of HS-PPM in our future work.

CRediT authorship contribution statement

Mingcan Zhao: Writing – original draft, Validation, Software, Methodology. **Feiguo Chen:** Writing – review & editing, Methodology. **Yu Zhang:** Writing – review & editing, Validation. **Chengxiang Li:** Writing – review & editing, Validation, Methodology. **Tianhao Qiu:** Validation. **Wei Ge:** Writing – review & editing, Supervision, Methodology, Funding acquisition, Conceptualization.

Declaration of competing interest

The authors declare that they have no known competing financial interests or personal relationships that could have appeared to influence the work reported in this paper.

Acknowledgements

This work was supported by the Key Program of the Chinese Academy of Sciences, the National Natural Science Foundation of China (Nos. 22293024, 22478390, 22178347, 22308359), and the IPE Project for Frontier Basic Research (No. QYJC-2022-001). This work was carried out using the facilities at Huairou Interdisciplinary Research Center for Mesoscience, CAS-IPE. The authors gratefully acknowledge the support and help from Huihuang Xia, Qi Zhao, Hui Li, and Linbo Ma of the State Key Laboratory of Mesoscience and Process Engineering, Institute of Process Engineering, Chinese Academy of Sciences.

Appendix A. Supplementary data

Supplementary data to this article can be found online at https://doi.org/10.1016/j.partic.2026.06.002.

References

Akkaya, V. R., & Kandemir, I. (2015). Event-driven molecular dynamics simulation of hard-sphere gas flows in microchannels. *Mathematical Problems in Engineering, 2015*, Article 842837.
Allen, M. D., & Raabe, O. G. (1985). Slip correction measurements of spherical solid aerosol-particles in an improved millikan apparatus. *Aerosol Science and Technology, 4*, 269–286.
Bailey, A. B., & Hiatt, J. (1972). Sphere drag coefficients for a broad range of mach and reynolds-numbers. *AIAA Journal, 10*, 1436–1440.
Brzozowski, M., O'Brien, M., Ley, S. V., & Polyzos, A. (2015). Flow chemistry: Intelligent processing of gas-liquid transformations using a tube-in-tube reactor. *Accounts of Chemical Research, 48*, 349–362.
Chapman, S., & Cowling, T. G. (1970). *The mathematical theory of non-uniform gases* (3rd ed. ed.). Cambridge University Press.
Chen, G., & Boyd, I. D. (1996). Statistical error analysis for the direct simulation Monte Carlo technique. *Journal of Computational Physics, 126*, 434–448.
Chen, F. G., & Ge, W. (2010). Statistical properties of pseudo-particle systems. *Particuology, 8*, 332–342.
Cheng, N. S. (2009). Comparison of formulas for drag coefficient and settling velocity of spherical particles. *Powder Technology, 189*, 395–398.
Cheng, Y. S., Allen, M. D., Gallegos, D. P., Yeh, H. C., & Peterson, K. (1988). Drag force and slip correction of aggregate aerosols. *Aerosol Science and Technology, 8*, 199–214.
Davies, C. N. (1945). Definitive equations for the fluid resistance of spheres. In *Proceedings of the physical society of London* (Vol. 57, pp. 259–270).
Fedosov, D. A., Rogasinsky, S. V., Zeifman, M. I., Ivanov, M. S., Alexeenko, A. A., & Levin, D. A. (2004). Analysis of numerical errors in the DSMC method. In *24th*

international symposium on rarefied gas dynamics (RGD24) (Vol. 762, pp. 589–594). Monopoli, ITALY: Amer Inst Physics.
Figliola, N., Schmidt, D., & Lee, J. H. (2022). Pressure- and size-dependent aerodynamic drag effects on mach 0.3-2.2 microspheres for high-precision micro-ballistic characterization. *Applied Sciences-Basel, 12*, 9.
Ge, W., Chang, Q., Li, C. X., & Wang, J. W. (2019). Multiscale structures in particle-fluid systems: Characterization, modeling, and simulation. *Chemical Engineering Science, 198*, 198–223.
Ge, W., & Li, J. H. (2001). Macro-scale pseudo-particle modeling for particle-fluid systems. *Chinese Science Bulletin, 46*, 1503–1507.
Ge, W., & Li, J. H. (2003). Macro-scale phenomena reproduced in microscopic systems-pseudo-particle modeling of fluidization. *Chemical Engineering Science, 58*, 1565–1585.
Gokul, G., & Malaikannan, G. (2024). Insights into chemical kinetics of hybrid chemical reaction models in hypersonic rarefied flow. *Physics of Fluids, 36*.
Goswami, P., Baier, T., Tiwari, S., Lv, C., Hardt, S., & Klar, A. (2020). Drag force on spherical particle moving near a plane wall in highly rarefied gas. *Journal of Fluid Mechanics, 883*, 14.
Hou, C. F., Zhu, A. Q., Zhao, M. C., Zhang, S., Ye, Y. H., Huang, Y. F., Xu, J., & Ge, W. (2022). Atomistic simulation toward real-scale microprocessor circuits. *Chemical Physics Letters, 791*, Article 139389.
Hu, C., Bai, H., He, X., Zhang, B., Nie, N., Wang, X., & Ren, Y. (2017). Crystal MD: The massively parallel molecular dynamics software for metal with bcc structure. *Computer Physics Communications, 211*, 73–78.
Kandemir, I., & Sevilgen, F. E. (2008). Molecular dynamics simulation of helium-argon gas mixture under various wall conditions. *Molecular Simulation, 34*, 795–808.
Keel, A. G., Zapata, R. N., Passmore, R. D., & Kraige, L. G. (1972). Hypersonic low-density cone drag. *AIAA Journal, 10*, 561–562.
Kosyanchuk, V. V., & Yakunchikov, A. N. (2018). Simulation of gas separation effect in microchannel with moving walls. *Microfluidics and Nanofluidics, 22*, 8.
Kremmer, M., & Favier, J. F. (2001a). A method for representing boundaries in discrete element modelling - Part I: Geometry and contact detection. *International Journal for Numerical Methods in Engineering, 51*, 1407–1421.
Kremmer, M., & Favier, J. F. (2001b). A method for representing boundaries in discrete element modelling - Part II: Kinematics. *International Journal for Numerical Methods in Engineering, 51*, 1423–1436.
Li, Y. P., Zhang, C. L., Li, C. X., Liu, Z. C., & Ge, W. (2017). Simulation of the effect of coke deposition on the diffusion of methane in zeolite ZSM-5. *Chemical Engineering Journal, 320*, 458–467.
Li, Y. P., Zhao, M. C., Li, C. X., & Ge, W. (2017). Simulation study on the reaction-diffusion coupling in simple pore structures. *Langmuir, 33*, 11804–11816.
Li, Y. P., Zhao, M. C., Li, C. X., & Ge, W. (2019). Concentration fluctuation due to reaction-diffusion coupling near an isolated active site on catalyst surfaces. *Chemical Engineering Journal, 373*, 744–754.
Lindell, M., Hughes, S., Dixon, M., & Willey, C. (2006). Structural analysis and testing of the inflatable re-entry vehicle experiment (IRVE). In *47th AIAA/ASME/ASCE/AHS/ASC structures, structural dynamics, and materials conference 14th AIAA/ASME/AHS adaptive structures conference 7th* (p. 1699). American Institute of Aeronautics and Astronautics.
Liou, W. W., & Fang, Y. C. (2000). Implicit boundary conditions for direct simulation monte carlo method in MEMS flow predictions. *Cmes-Computer Modeling in Engineering & Sciences, 1*, 119–128.
Lu, J. X., Zhang, J. Y., Wang, X. W., Wang, L. M., & Ge, W. (2009). Parallelization of pseudo-particle modeling and its application in simulating gas-solid fluidization. *Particuology, 7*, 317–323.
Ma, L. B., Zhao, M. C., Zhao, Q., Cui, L. J., Chen, F. G., & Ge, W. (2019). Simulation of flow around a single sphere at low mach numbers by hard sphere/pseudo particle modeling (HS-PPM). *Computers and Applied Chemistry, 36*, 439–444.
Mailler, S., Menut, L., Cholakian, A., & Pennel, R. (2023). Aersett v1.0: A simple and straightforward model for the settling speed of big spherical atmospheric aerosols. *Geoscientific Model Development, 16*, 1119–1127.
Marin, M. (1997). Event-driven hard-particle molecular dynamics using bulk-synchronous parallelism. *Computer Physics Communications, 102*, 81–96.
Moss, J., Glass, C., Hollis, B., & Norman, J. V. (2006). Low-density aerodynamics for the inflatable reentry vehicle experiment. *Journal of Spacecraft and Rockets, 43*, 1191–1201.
O'Keefe, S., & Bose, D. (2010). IRVE-II post-flight trajectory reconstruction. In *AIAA atmospheric flight mechanics conference* (p. 7515). American Institute of Aeronautics and Astronautics.
Olds, A., Beck, R., Bose, D. M., White, J., Edquist, K. T., Hollis, B. R., Lindell, M., Cheatwood, F., Gsell, V., & Bowden, E. L. (2013). IRVE-3 post-flight reconstruction. In *AIAA aerodynamic decelerator systems (ADS) conference* (p. 1390). American Institute of Aeronautics and Astronautics.
Pieprzyk, S., Branka, A. C., Heyes, D. M., & Bannerman, M. N. (2024). Revised enskog theory and molecular dynamics simulations of the viscosities and thermal conductivity of the hard-sphere fluid and crystal. *Physical Review E, 109*, 21.
Plimpton, S. J., Moore, S. G., Borner, A., Stagg, A. K., Koehler, T. P., Torczynski, J. R., & Gallis, M. A. (2019). Direct simulation monte carlo on petaflop supercomputers and beyond. *Physics of Fluids, 31*, 18.
Plotnikov, M. Y., & Shkarupa, E. V. (2010). Some approaches to error analysis and optimization of the DSMC method. *Russian Journal of Numerical Analysis and Mathematical Modelling, 25*, 147–167.
Plotnikov, M. Y., & Shkarupa, E. V. (2012). Comparison of different approaches to evaluation of statistical error of the DSMC method. In *28th international symposium on rarefied gas dynamics (RGD)* (pp. 503–510). Zaragoza, SPAIN: Amer Inst Physics.
Qiu, T. H., Zhao, M. C., Li, Y. P., Li, C. X., & Ge, W. (2022). Multiscale modeling of gas-solid surface interactions under high-temperature gas effect. *Journal of Thermophysics and Heat Transfer, 36*, 951–963.
Ramirez, C. A. (2017). Summary of frictional drag coefficient relationships for spheres: Evolving solution strategies applied to an old problem. *Chemical Engineering Science, 168*, 339–343.
Ramirez, R., Risso, D., & Cordero, P. (2000). Thermal convection in fluidized granular systems. *Physical Review Letters, 85*, 1230–1233.
Scalas, E., Gabriel, A. T., Martin, E., & Germano, G. (2015). Velocity and energy distributions in microcanonical ensembles of hard spheres. *Physical Review E, 92*, Article 022140.
Schaaf, S. A., & Chambré, P. L. (1961). *Flow of rarefied gases*. PRINCETON UNIVERSITY PRESS. PRINCETON, NEW JERSEY.
Shah, N., Gavasane, A., Agrawal, A., & Bhandarkar, U. (2018). Comparison of various pressure based boundary conditions for three-dimensional subsonic DSMC simulation. *Journal of Fluids Engineering-Transactions of the Asme, 140*, 12.
Shen, Q. Y., Zhang, C., Tahir, M. F., Jiang, S. K., Zhu, C. Y., Ma, Y. G., & Fu, T. T. (2018). Numbering-up strategies of micro-chemical process: Uniformity of distribution of multiphase flow in parallel microchannels. *Chemical Engineering and Processing: Process Intensification, 132*, 148–159.
Sun, Q., Xie, F., Zhao, G., Peng, W., Wang, J., & Yu, S. Y. (2018). A numerical study on slip correction factor of dust particle in htgr. *Nuclear Engineering and Design, 340*, 31–39.
Sun, M. H., Zhou, J., Hu, Z. Y., Chen, L. H., Li, L. Y., Wang, Y. D., Xie, Z. K., Turner, S., Van Tendeloo, G., Hasan, T., & Su, B. L. (2020). Hierarchical zeolite single-crystal reactor for excellent catalytic efficiency. *Matter, 3*, 1226–1245.
Suryawanshi, P. L., Gumfekar, S. P., Bhanvase, B. A., Sonawane, S. H., & Pimplapure, M. S. (2018). A review on microreactors: Reactor fabrication, design, and cutting-edge applications. *Chemical Engineering Science, 189*, 431–448.
Tao, S., & Guo, Z. L. (2017). Gas-solid drag coefficient for ordered arrays of monodisperse microspheres in slip flow regime. *Chemical Engineering & Technology, 40*, 1758–1766.
Tao, S., Zhang, H. L., & Guo, Z. L. (2017). Drag correlation for micro spherical particles at finite reynolds and knudsen numbers by lattice boltzmann simulations. *Journal of Aerosol Science, 103*, 105–116.
Tchipev, N., Seckler, S., Heinen, M., Vrabec, J., Gratl, F., Horsch, M., Bernreuther, M., Glass, C. W., Niethammer, C., & Hammer, N. (2019). Twetris: Twenty trillion-atom simulation. *International Journal of High Performance Computing Applications, 33*, 838–854.
Tian, Y. H., Lin, G. P., Guo, J. H., & Zhang, Q. M. (2025). Permeability of porous microstructure in thermal protection system under high-temperature reactive gas conditions. *Physics of Fluids, 37*, 15.
Tian, S. Y., & Wu, L. (2024). Multiscale modelling and simulation of coexisting turbulent and rarefied gas flows. *Journal of Fluid Mechanics, 1002*, 23.
Voronin, F. S., & Zhdanova, L. N. (1987). Drag of a slender cone in a supersonic rarefied gas flow. *J Fluid Dynamics, 22*, 163–166.
Watanabe, H., Suzuki, M., & Ito, N. (2013). Huge-scale molecular dynamics simulation of multibubble nuclei. *Computer Physics Communications, 184*, 2775–2784.
Wegner, J., Ceylan, S., & Kirschning, A. (2012). Flow chemistry - A key enabling technology for (multistep) organic synthesis. *Advanced Synthesis & Catalysis, 354*, 17–57.
Wu, L., Liu, H. H., Reese, J. M., & Zhang, Y. H. (2016). Non-equilibrium dynamics of dense gas under tight confinement. *Journal of Fluid Mechanics, 794*, 252–266.
Wu, J., Xu, Q. Y., Zhang, Z., & Hou, A. P. (2022). Aeroelastic characteristics of inflatable reentry vehicle in transonic and supersonic regions. *Computers & Fluids, 237*, Article 105338.
Wu, L., Zhang, Y. H., & Reese, J. M. (2015). Fast spectral solution of the generalized enskog equation for dense gases. *Journal of Computational Physics, 303*, 66–79.
Yakunchikov, A., & Kosyanchuk, V. (2018). Application of event-driven molecular dynamics approach to rarefied gas dynamics problems. *Computers & Fluids, 170*, 121–127.
Yakunchikov, A., & Kosyanchuk, V. (2019a). A new principle of separation of gas mixtures in non-stationary transitional flows. *Acta Astronautica, 163*, 120–125.
Yakunchikov, A., & Kosyanchuk, V. (2019b). Numerical investigation of gas separation in the system of filaments with different temperatures. *International Journal of Heat and Mass Transfer, 138*, 144–151.
Yakunchikov, A., Kosyanchuk, V., Filatyev, A., & Golikov, A. (2025). Simulation of rarefied gas flow inside the satellite air intake in ultra-low Earth orbit. *Acta Astronautica, 226*, 102–112.
Yamamoto, K., Takeuchi, H., & Hyakutake, T. (2006). Characteristics of reflected gas molecules at a solid surface. *Physics of Fluids, 18*, Article 046103.
Zhang, C. L., Shen, G. F., & Ge, W. (2016a). Simulation of supersonic flow with hard-sphere/pseudo-particle modeling (HS-PPM). *Computers and Applied Chemistry, 33*, 1135–1144.
Zhang, C. L., Shen, G. F., Li, C. X., Ge, W., & Li, J. H. (2016b). Hard-Sphere/Pseudo-Particle modelling (HS-PPM) for efficient and scalable molecular simulation of dilute gaseous flow and transport. *Molecular Simulation, 42*, 1171–1182.
Zhao, Q., Zhao, M. C., Ma, L. B., & Ge, W. (2019). Hard-Sphere/Pseudo-Particle modeling (HS-PPM) for hypersonic rarefied gas flow. *The Chinese Journal of Process Engineering, 19*, 1093–1100.
Zhu, C. Y., Lu, Y. T., Fu, T. T., Ma, Y. G., & Li, H. Z. (2017). Experimental investigation on gas-liquid mass transfer with fast chemical reaction in microchannel. *International Journal of Heat and Mass Transfer, 114*, 83–89.